TECHNISCHE UNIVERSITÄT MÜNCHEN

Fakultät für Informatik
I–16 / Computer Aided Medical Procedures

Computational modeling of detection physics for 3D intraoperative imaging with navigated nuclear probes

Alexander Olavi Hartl

Vollständiger Abdruck der von der Fakultät für Informatik der Technischen Universität München zur Erlangung des akademischen Grades eines

Doktors der Naturwissenschaften (Dr. rer. nat.)

genehmigten Dissertation.

Vorsitzender:	Univ.-Prof. Dr. K. A. Kuhn
Prüfer der Dissertation:	
1.	Univ.-Prof. Dr. N. Navab
2.	apl. Prof. Dr. S. Ziegler

Die Dissertation wurde am 09.06.2015 bei der Technischen Universität München eingereicht und durch die Fakultät für Informatik am 29.10.2015 angenommen.

"It's not about how many stocks you have, it's about how much copper wire you can get out of the building with!"

The Simpsons

Abstract

Today we can look at and into patients with many different modalities. We are able to produce 3D images of the patient's body with incredible accuracy and we can even image functions within the body. These imaging techniques are extremely helpful for diagnostics. However in intra-operative settings most of these imaging techniques suffer from severe drawbacks. They are either not flexible enough or too big to be used during surgery and they often have too high acquisition times. This leads to a huge gap between information that physicians have access to in diagnostics and surgery.

Freehand SPECT is a novel imaging modality which was specifically designed for the intra-operative setting. It is a functional imaging modality, employing radioactive tracers which follow a specific metabolic pathway in the patient's body. The device consists of a hand held nuclear probe to detect the radiation of the tracer and an optical tracking system to obtain the position and orientation of the probe simultaneously with its readings. The combined information can then be used to compute a tomographic reconstruction of the radiation distribution.

However in contrast to conventional tomographic systems there is no fixed acquisition geometry and thus the system matrix for the reconstruction has to be build up on the fly. Additionally acquisition geometries are dependent on the user and have a huge impact on the reconstruction quality.

In this thesis models of the detection process of the probe to generate the system matrix on the fly are presented, as well as a method to optimize acquisition geometries to improve the reconstruction quality. Three different models were developed and evaluated. Two of the models try to compute analytically the contribution of a source to a reading of the probe with different levels of complexity. The third model is a look up table that is either generated from acquired measurements with the probe or from Monte Carlo simulations.

A simulation framework is also used to generate, simulate and reconstruct different acquisitions geometries for a known activity distribution. This can be used to find an optimal acquisition geometry for surgery when diagnostic images are available.

Zusammenfassung

Heutzutage können wir Patienten und deren Inneres mit vielen verschiedenen Modalitäten betrachten. Wir können 3D Bilder vom Körper des Patienten mit unglaublicher Genauigkeit erstellen und wir können sogar Funktionen im Körper des Patienten in Bildern aufnehmen. Diese bildgebenden Methoden sind extrem hilfreich in der Diagnostik. Im intra-operativen Bereich leiden diese Techniken allerdings unter schwerwigenden Problemen. Sie sind entweder nicht flexibel genug oder viel zu gro für den OP oder die benötigten Aufnahmezeiten sind einfach viel zu lang. Das führt zu einer groen Lücke an Information die man im OP im Vergleich zur Diagnostik zur Verfügung hat.

Freehand SPECT ist eine neue bildgebende Technik die speziell für das intra-operative Umfeld entwickelt wurde. Es ist ein bildgebendes Mittel das radioaktive Tracer nutzt, die im Körper des Patienten einen bestimmten metabolischen Pfad folgen. Das System besteht aus einer in der Hand gehaltenen Sonde welche die radioaktive Strahlung des Tracers messen kann und aus einem optischen Tracking System um die Position und Orientierung der Sonde gleichzeitig mit den Messwerten zu erhalten. Diese kombinierten Daten können verwendet werden um eine tomographische Rekonstruktion der Verteilung der Radioaktivität zu berechnen.

Im Gegensatz zu konventionellen tomographischen Systemen verfügt Freehand SPECT allerdings nicht über eine fixe Akquisitionsgeometrie, weshalb die System Matrix immer neu berechnet werden muss. Zudem sind Akquisitionsgeometrien abhängig vom Nutzer und haben einen groen Einfluss auf die Qualität der Rekonstruktionen.

In dieser Arbeit werden Modelle des detektions Prozesses um die System Matrix schnell neu zu berechnen vorgestellt sowie eine Methode um die Akquisitionsgeometrie zu optimieren um die Rekonstruktions Qualität zu verbessern. Drei verschiedene Modelle wurden entwickelt und evaluiert. Zwei der Modelle versuchen analytisch zu berechnen welchen Einfluss eine Punktquelle auf eine Messung hat. Das dritte Modell ist eine Nachschlagetabelle von Messwerten welches entweder durch reale Messwerte einer Sonde oder durch Monte Carlo Simulationen erstellt wird.

Eine Simulationsumgebung wird ebenfalls verwendet um verschiedene Akquisitionsgeometrien bei einer bekannten Verteilung von Radioaktivität zu erstellen, zu simulieren und zu rekonstruieren. Diese Methode kann verwendet werden um Akquisitionsgeometrien für Operationen zu optimieren wenn diagnostische Aufnahmen verfügbar sind.

Acknowledgements

Over the course of this work I had the privilege of working together, getting advice and help from a lot of persons without whom this work would not have been possible. First I have to mention Tobias Lasser who was guiding me on the path of my PhD. His constant advice and help was absolutely crucial to finish my work and I really appreciate that I had the chance to work with him as a colleague, group supervisor and friend. Thanks for everything and keep the great work up you're doing.

I also want to thank my other colleagues from the NaNu group who were in the one or other way always directly involved in my work. Dzhoshkun, with whom I collaborated very closely in all my works and I spent a lot of time together at conferences and nights full of work, it was great to work together with you. Asli you were several times my savior when it came to evaluating all the stuff I had done, I was very grateful to profit from the work you had done for your evaluations and your help to get data from phantoms and patients. In such a work as mine there is always a lot of stuff that needs to be build and set up in order to get from theory to some real results and it's hard to say how grateful I am that we had just the man to do that in our group. Thank you Jos. The discussions I had with Philipp were very helpful to get to some insights during my work and of course I want to thank all of you for the good time and laughs we had at our work in the lab. It was really great to work with such colleagues and friends.

I also want to thank Thomas Wendler, who was my first supervisor in this field of work and who introduced me to this exciting world. His style of supervision was distinctly different from Tobias's, but nonetheless it was great to have had him as supervisor and friend. Also the constant collaboration with his company SurgicEye was very important to be able to actually do this work. Thanks for all that and thanks to all guys from SurgicEye.

I am also very grateful for my two supervisors in this work Prof. Nassir Navab and Prof. Sibylle Ziegler who gave me the chance and necessary support to do my research in this field. To profit from their vast knowledge and experience made things a lot easier for me and also the chance to learn about so much more than only the things concerning my thesis was a great experience which I really appreciate.

The whole CAMP chair also deserves a lot of thanks from me. It was great to discuss with all the people at the chair and learn all their works. More than one time I got just the inspiration or advice I needed to go on with my work. I had a great time working with all of you.

Last but not least I want to thank Melanie, Jozef, Florian and Rebekka for their company and help during the long hours in the lab.

Contents

Abstract v

Zusammenfassung vii

Acknowledgements ix

1 Introduction 1
- 1.1 Medical vision . . . 1
- 1.2 Anatomical Medical Imaging Modalities . . . 2
  - 1.2.1 X–ray imaging . . . 2
  - 1.2.2 X–ray computed tomography . . . 4
  - 1.2.3 Ultrasound . . . 4
  - 1.2.4 Magnetic resonance imaging . . . 4
- 1.3 Functional Medical Imaging Modalities . . . 6
  - 1.3.1 Probes . . . 6
  - 1.3.2 Cameras . . . 8
  - 1.3.3 Single photon emission computed tomography . . . 8
  - 1.3.4 Positron emission tomography . . . 9
- 1.4 Tracers . . . 10
  - 1.4.1 Compartment model . . . 10
  - 1.4.2 Gamma ray emitting tracers . . . 12
  - 1.4.3 Positron emitting tracers . . . 13
- 1.5 Tomography . . . 13
- 1.6 Intra-operative functional imaging . . . 15
- 1.7 Thesis Outline . . . 18

2 Modeling of detection physics 19
- 2.1 The detection process . . . 20
  - 2.1.1 Radioactive decay . . . 21
  - 2.1.2 Solid angle . . . 22
  - 2.1.3 Photoelectric effect . . . 23
  - 2.1.4 Compton scattering . . . 24
  - 2.1.5 Pair production . . . 25
  - 2.1.6 Background noise . . . 25
- 2.2 State of the art . . . 26

2.2.1 Analytical modeling . . . 27
2.2.1.1 Intrinsic, septal penetration and septal scatter response . . . 27
2.2.1.2 Geometric response . . . 28
2.2.2 Monte Carlo simulations . . . 33
2.2.2.1 GEANT4 . . . 34
2.2.2.2 GATE . . . 34
2.2.3 Direct measurements . . . 35
2.2.4 Methods in comparison . . . 35

3 Models of detection physics for Freehand SPECT 37
3.1 Solid angle model . . . 37
3.1.1 Detection of gamma rays . . . 40
3.2 Partition model . . . 40
3.2.1 Effects of the geometry . . . 41
3.2.2 Detection . . . 41
3.2.3 Shielding . . . 44
3.2.3.1 Photoelectric effect . . . 44
3.2.3.2 Compton scattering . . . 44
3.2.4 Summary . . . 46
3.3 Look up table . . . 47
3.4 Experiments and results . . . 48
3.4.1 Models in Comparison . . . 48
3.4.2 Experiments . . . 50
3.4.3 Evaluation . . . 51
3.4.4 Results . . . 52

4 Simulating and optimizing acquisition geometries 61
4.1 Simulation of Freehand SPECT . . . 61
4.1.1 GATE . . . 62
4.2 Error measure for reconstructions . . . 62
4.3 Optimization process . . . 64
4.4 Experiments and results . . . 65
4.4.1 Simulations . . . 65
4.4.2 Results . . . 65

5 Discussion and Conclusions 67
5.0.3 Discussion . . . 67
5.0.4 Conclusions . . . 68

A List of Publications 69
A.1 Submitted Journal Publications . . . 69
A.2 Conference publications . . . 69

Bibliography 73

Chapter 1

Introduction

1.1 Medical vision

Since the beginning of medicine visual information has been an important tool for the treatment of patients. The vision of a physician was for a long time the only kind of such information and could be regarded as the first kind of medical imaging. The first developments in medical imaging aimed for an improvement of the vision of a physician by using additional light sources and magnifying lenses. This lead finally to the invention of microscopy which today allows especially the investigation of tissue samples for diagnostic purposes.
However the vision of a physician is still almost completely limited to the surface of an object, and in order to see what is inside a patient for a long time the only way was to cut the patient open. This was usually not desirable as this might have caused more harm than good and in the worst case it might have caused the death of the patient.
In 1895 when a German physicist accidentally discovered how to image the attenuation of high energetic electromagnetic waves in material, it became possible to see through an object [1]. With the discovery of the X–rays by Willhelm Conrad Röntgen the field of medical imaging was revolutionized. X–rays made it finally possible to see the inside of a patients body without opening it.

Especially for the diagnosis of many diseases the knowledge of what's going on inside of the patients body is necessary, but also for the industry it is extremely helpful to learn what is inside of an object without the need to open it. Thus imaging technology that can provide images of the inside of an object are extremely valuable.
However X–ray imaging on its own can only provide 2D images and no depth information. Thus the next step was to get 3D information of the insides of an object which became

Figure 1.1: One of the first X–ray images, showing the hand of Willhelm Conrad Röntgen's wife Anna.

possible with the development of tomographic imaging by Godfrey N. Hounsfield in 1972 [2].
This was not the end of developments in medical imaging but instead started a huge wave of innovations in medical imaging and tomography. Today we have many different kinds of medical imaging modalities, which we can separate into two groups.
Anatomical imaging gives us information of the structures inside of a patient while functional imaging gives us information about what is happening in the patient.

1.2 Anatomical Medical Imaging Modalities

Anatomical imaging is the kind of medical imaging most people are aware of. They show us the structures inside of a patient and the most prominent modality there is probably the X–ray imaging mentioned before.

1.2.1 X–ray imaging

X–rays are ionizing radiation which are able to penetrate through material while a certain amount of it is absorbed, depending on the density of the material. A X–ray source is positioned in front of an object and a detector plate is placed on the opposite side. On the detector plate the attenuation image of the object becomes then visible.

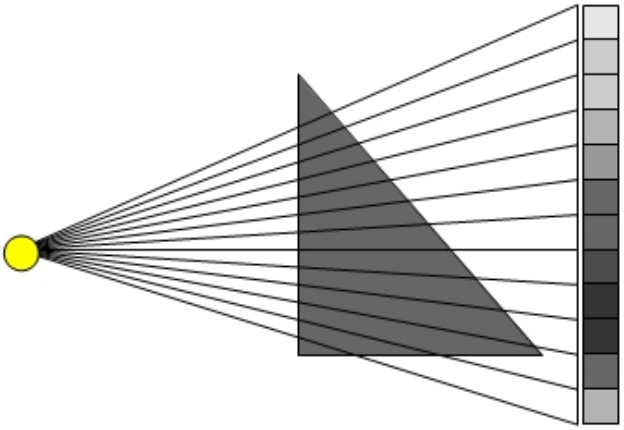

Figure 1.2: An object is placed between a x–ray source and a detector plate. On the detector the attenuation image of the object becomes visible.

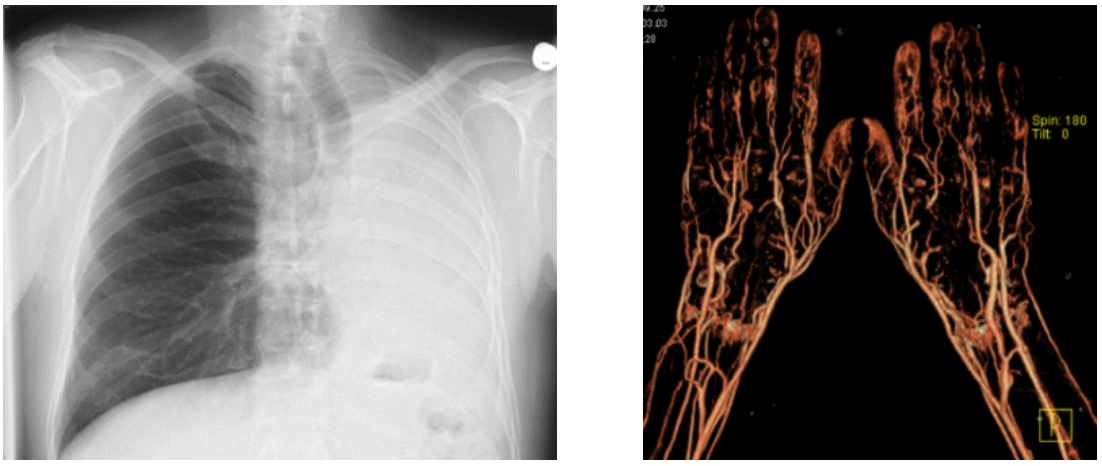

Figure 1.3: X–ray image of the thorax (left) and an angiographic x-ray image of the hands (right).

This allows the examination of the insides of an object or a patients body [3]. The attenuated radiation is however harmful for the patient and although the doses used for X–ray imaging are too low for an instant deterministic effect there is always a probability for a non deterministic effect which might result for example in cancer.
As the images obtained by X–rays are effectively density images they are mainly used to image bones, however by employing contrast agents, which have a high density, also vessels can be imaged. Besides X–ray imaging there are many other different anatomical imaging modalities which have different uses and can give better information of other structures in the body of a patient.

1.2.2 X–ray computed tomography

X–ray imaging can also be extended to 3D imaging with the use of computed tomography (CT). X–ray computed tomography was the first tomographic system and was developed 1971 by Sir Godfrey Hounsfield [2]. The tomographic image is obtained by rotating a X–ray source and detector plate around the patient while continuously acquiring images. Different scanning geometries include parallel beam geometries where the x–rays traverse the object on parallel trajectories and fan beam geometries where the x–rays are emitted from a point and cover the object in a fan of x–rays. The latter was used to reduce the scanning time and was further developed to the cone beam geometry by using a 2D detector. Using the whole set of images a mathematical reconstruction can be performed to obtain a 3D Volume of density related values.
In modern x–ray CT devices the x–ray source and the detectors are arranged in a gantry and do spiral or helical scans of the patient. Usually the cone beam geometry is used with scanning times of several seconds and an accuracy in the submilimeter region. X–ray CT allows for a more accurate examination of the patient and makes it even possible examine soft tissue to a certain degree, however the radiation dose also becomes higher than in conventional X–ray imaging.

1.2.3 Ultrasound

In Ultrasound imaging we can see the reflections of ultrasound in the body, such reflections occur especially when the matter the ultrasound penetrates changes. For ultrasound imaging a hand held probe with an array of ultrasound transducers is used which generates a planar image of the tissue in front of the probe. This makes it possible to examine tissue regardless of its density, so it is often used for soft tissue imaging [4].
In addition ultrasound is harmless for the patient so an examination bears no additional risks and the costs for using ultrasound are also very low.
The downside of ultrasound is that its usage is difficult and the images are hard to interpret. Thus the result of the examination is directly depended on the experience of the user. With recent developments 3D ultrasound became available. By not only imaging a single plane but a volume the usage of ultrasound also becomes more simple.

1.2.4 Magnetic resonance imaging

Another tomographic imaging modality is magnetic resonance imaging (MRI). This imaging technique uses magnetic fields to generate signals that depend on the material that is placed

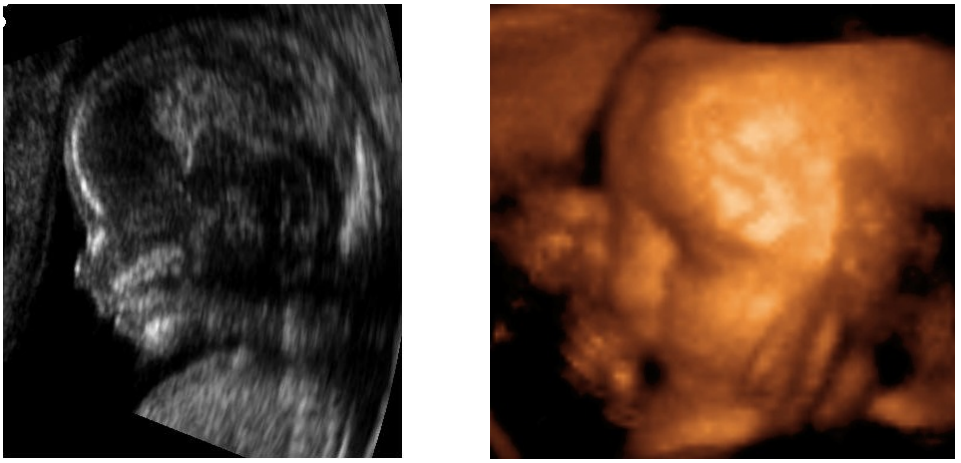

Figure 1.4: Ultrasound images of a fetus. Left conventional Ultrasound, right 3D Ultrasound.

inside the magnetic fields. It employs the fact that protons inside a nucleus are spinning and as a charged particles they are therefore generating a magnetic momentum.
When an object is placed in a strong constant magnetic field the spinning axes of the protons will align on the direction of the magnetic field. Other magnetic fields are then used to tip the spinning axes of the protons by being turned on and then off again. The spinning axes will then again align themselves in the direction of the constant magnetic field. This movement will induce an electrical signal in receiver coils which are placed around the patient. Using these signals a tomographic reconstruction of the object can be performed [5].
In 1973 the first magnetic resonance images were published and in 2003 Paul Lauterbur and Sir Peter Mansfield were awarded with the Nobel Prize in Medicine for their work on magnetic resonance imaging. However this raised some controversies as the contributions of the physicist Herman Carr and the physician Raymond Damadian were not considered by the Nobel Prize committee.
The signals generated with MRI are depended on the proton density which makes it possible to examine in MRI different structures than in X–ray CT. Especially for soft tissue examination MRI is better suited. Another advantage of MRI is that it is not using ionizing radiation, however the image acquisition takes much longer. MRI image acquisitions take two to three hours for a whole body scan, however typically only parts of the body are scanned which takes usually something around 30 minutes. Another limitation lies in the fact that inside the room with the Magnetic Resonance Scanner there must not be any magnetic objects as such might become dangerous missiles in the strong magnetic fields of the scanner.

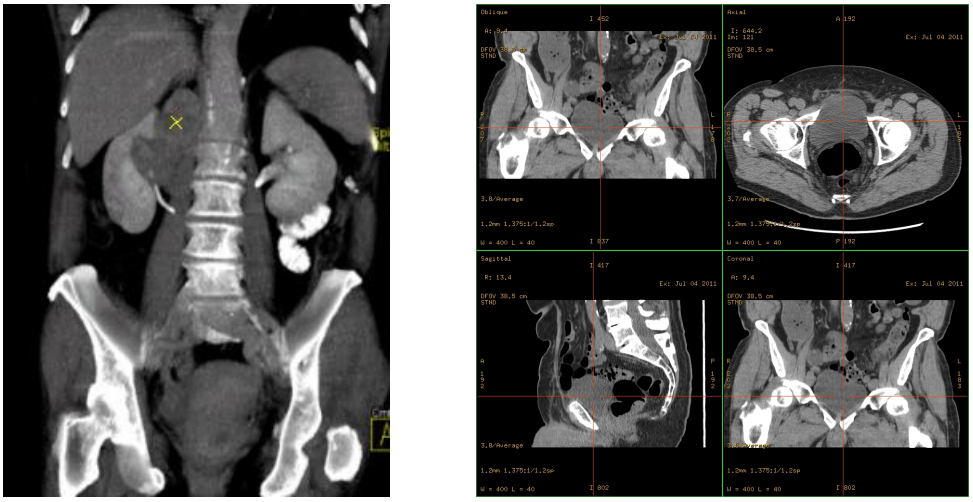

Figure 1.5: Tomographic images. Left CT, right MRT.

1.3 Functional Medical Imaging Modalities

In contrast to anatomical imaging functional imaging usually doesn't provide information about the structures of the body. Instead with functional imaging functions of the body can be observed. This is usually done by injecting a so called tracer to the patient. The tracer is a substance which follows a certain metabolic pathway and by imaging the tracer its metabolism in the patient is also revealed.
A common way to image a tracer is by attaching a radioactive isotope to its molecule, imaging using such radioactive tracers is also called nuclear imaging. With a radiation detector the tracer can then be found inside the patient.

1.3.1 Probes

A single detector in a hand held probe can be used to pinpoint large accumulations of radiation in the patient, however it doesn't really provide images and cannot be used for an accurate examination. Instead probes are used during surgery to guide the surgeon
The idea of using radiation detectors in surgery to guide the surgeon during the intervention came up approximately 60 years ago. In 1949 the first study using a Geiger-Müller tube was conducted on brain tumor patients. The first radio guided surgery using a gamma detection probe was reported by Harris et al in 1956.
There are two different types of probes used in surgery, based upon the type of radiation they can detect. Gamma probes are used to detect photon radiation with high energies, usually gamma radiation and x–ray radiation. Beta probes are used to detect beta radiation which are either electrons or positrons [6]. The use of the probe thus depends on the used

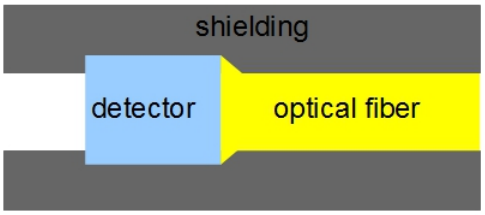

Figure 1.6: A nuclear probe to detect gamma radiation (left), schematic of a slice through a gamma probe.

tracer.

The quality of a probe depends on several characteristics, which are of different importance depending on the procedure they are going to be used for. Sensitivity describes the amount of counts produced from a unit activity and is important to get statistically reliable results from the probe. The spatial selectivity describes the size of the conic volume in front of the probe from where counts will be measured. The larger this volume is the less specific the measurement is which makes it more difficult to find a source of activity. The spatial resolution describes how well the probe can localize sources and distinguish between sources which are close together. The energy resolution is the ability to discriminate radiation of different energies. This is important to distinguish between the radiations of different radionuclides or between scattered and unscattered radiation. Last the contrast, describing the ability to distinguish between target and background radiation, is an important factor for probes.

For the detector itself there are again two different categories used in current probes, scintillators and semiconductors. The basic principle of a scintillating detector is that radiation that passes through the detector excites atoms in the scintillator. Then the excited atoms emit light which is transformed to an electrical signal with a photomultiplier. In semiconductors the radiation emitted by a source produces free electrons and these electrons are then used to generate a signal. Scintillation based probes have a higher sensitivity than semiconductor based probes, however they also have a worse energy resolution and the probes are usually bulkier.

The choice of the probe for a certain procedure depends on different factors. One of the most important ones is the size, weight and ergonomics of the probe as its use has to be comfortable for the surgeon. Sensitivity is crucial when only low doses of a tracer are used and contrast becomes extremely important when the used tracer is not very specific. The spatial resolution is important when many different targets have to be localized and the spatial specifity is of high importance when we have high radiation areas (for example the injection site of the tracer) close to our target.

1.3.2 Cameras

In 1957 the first gamma camera was developed by Hal Anger. In his original design, which is still often used today, an array of photomultipliers is placed behind a scintillator. When a gamma ray interacts in the scintillating crystal the emitted light reaches the photomultipliers with different degrees of intensity, depending on their position relative to the location of the interaction. Each photomultiplier will then generate a signal with different strength. Using these signals the location of the interaction can be estimated. The gamma camera can thus provide spatial information by a 2D image of the detected events.
A collimator is used in front of the detectors to limit the direction from where radiation is detected and to define the field of view of the camera. Making it easier to localize the source of the detected events and thus enhance the accuracy, however sensitivity is lost as a lot of radiation will be absorbed in the collimator. Different collimators are used for different imaging tasks. Parallel hole collimators are used to obtain images of the same size as the object and are the most common type of collimator. Pinhole collimators can be used to magnify a region of interest, however the field of view will be limited. Another way to obtain a magnification is by using a converging hole collimator. Using a collimator with diverging holes, the field of view can be increased but the observed region is minified on the image.
Other designs for gamma cameras use separate detector elements so no additional computation is needed to get the 2D location of the event.
Initially gamma cameras were mainly used in diagnostics, however due to the ongoing miniaturization gamma cameras can be built very small and lightweight. Such smaller gamma cameras can be used in an intra–operative setting similar to gamma probes.
As with probes also cameras to detect beta radiation were developed.

1.3.3 Single photon emission computed tomography

Single Photon Emission Computed Tomography (SPECT) is a functional imaging method able to generate 3D images of a radiation distribution [8, 9]. Radiotracers based on gamma ray emitting nuclides are employed for SPECT. A commonly used radioactive isotope used in SPECT is Tc99m, which emits gamma rays with a mean energy of 140.51 keV. The radioactive nuclide is attached to a radio–ligand which is used to define the function that can be imaged with the resulting radiotracer.
The SPECT device consists of gamma cameras that are rotated around the patient. The acquired data can then be processed with a reconstruction algorithm to compute a 3D distribution of the radiation. Collimation is here even more important as solving the reconstruction problem gets easier the more limited the space is where the detected radiation

Figure 1.7: Gamma Cameras provide 2D images of radiation distributions and are used for diagnostics and as guidance during surgery [7].

came from.
The first SPECT devices were developed in the early 1960s and experienced a lot of developments to improve the device. Most notably is the combination with CT in a single device so both functional and anatomical images can be acquired with the images being rigidly coregistered. This solves one of the major problems of functional imaging: the missing anatomical context of the images. In addition the CT image is used for attenuation correction in the patients body to improve the SPECT image quality.

1.3.4 Positron emission tomography

Another form of tomographic functional imaging doesn't require collimation. Positron Emission Tomography (PET) uses radioactive tracers that emit positrons [8]. When a positron hits an electron both will annihilate and produce two gamma rays in opposite directions with a distinctive energy of 511 keV. This will usually happen within a distance of 2mm from the emitting molecule.
In PET a ring of detectors is used to detect these annihilation gamma rays. Whenever two gamma rays with the distinctive energy are detected, within a small time window, these rays are regarded to come from the same annihilation process. The annihilation process must then have occurred on a so called line of response which is drawn between the two detectors.
More advanced PET systems use in addition a technique called time of flight (TOF). Here the difference in time for the detection of both gamma rays is used to compute a more

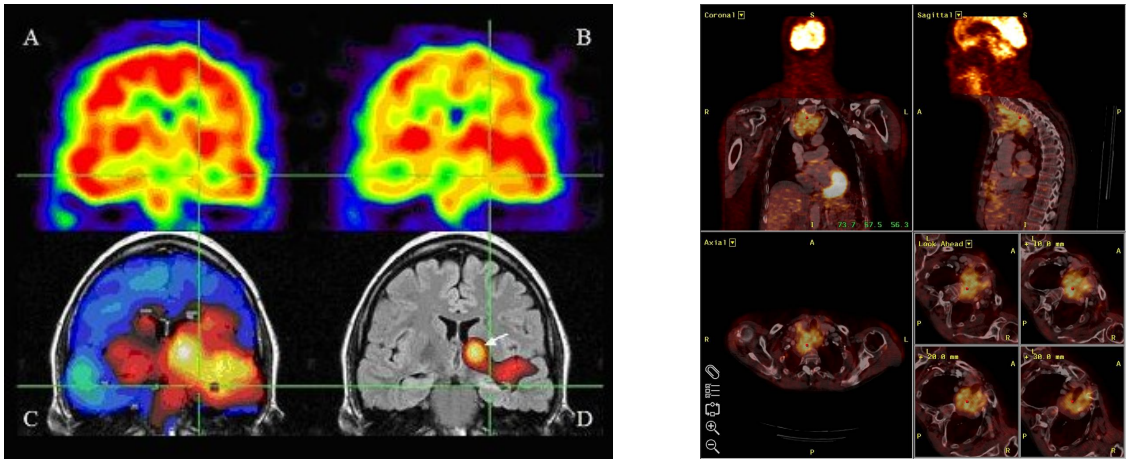

Figure 1.8: SPECT image of the brain (left) and a PET of the upper part of the body (right). Both imaging modalities are fused with a CT image of the respective regions.

accurate location on the line of response. In both cases the collected data is used in a tomographic reconstruction which then yields the 3D distribution of the radioactive tracer. Due to the missing anatomical information to put the functional images into a context both SPECT and PET are usually combined with a CT and in the recent past machines that combine PET and MRI were developed.

1.4 Tracers

Nuclear imaging relies upon the use of radioactive substances called tracers. These substances consist of two parts, the first part is a molecule which is processed in the human body in a known way. For the second part a radioactive isotope is needed to replace a part of the initial molecule without changing how it is processed in the human body. This is the so called tracer principle which was discovered in 1912 by the hungarian chemist George de Hevesy, who was awarded with the nobel prize for his work on radioactive tracers in 1943. The radioactive part of the substance can then be observed by a radiation detector, which then allows us to image the metabolic pathway taken by the substance.

1.4.1 Compartment model

For the use of tracers the knowledge how it will distribute it in the human body is thus of high importance. The metabolic pathway taken by tracers is usually modeled by a so called compartment model [10]. In this model the physiologic system of the human body is decomposed into a number of interacting subsystems, the compartments. As the used amounts of tracer material is very small we assume that it does not influence the system we

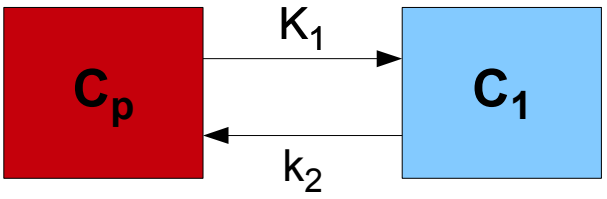

Figure 1.9: The one tissue compartment model. C_1 is the tracer concentration in the tissue compartment and is increased over a transfer from the blood depending on the tracer concentration in the blood flow C_p. In a reverse process the tiusse is also transfering tracer back into the blood flow.

are looking at.
For the transport of the tracer between the compartments a first order process is assumed to allow for a reasonable computation with standard mathematical models. The change of the tracer concentration in every compartment can thus be described by a linear function of the tracer concentrations in the other compartments.
The most simple model only includes only one tissue compartment, thus it is called a one tissue compartment model (1TCM Figure 1.9).

In this model we only consider the tracer concentrations in the target tissue and in the blood, which is assumed to be the same throughout the body due to mixing in the blood flow. The tracer concentration in the tissue $C_1(t)$ increases due to extraction from the blood. Another typical restriction for the model is that only the unchanged tracer (authentic tracer) that was not metabolised yet can enter the tissue. The extraction is described by a first-order process which results in the transfer being proportional to the authentic tracer concentration $C_p(t)$. Conversely the tracer concentration in the tissue is reduced by a backward transfer which follows the same mechanics. Both processes compete with each other so the change of the tracer concentration over time can be described by a differential equation:

$$\frac{dC_1(t)}{dt} = K_1 C_p(t) - k_2 C_1(t) \tag{1.1}$$

K_1 and k_2 are transfer coefficients: K_1 is perfusion dependent and describes the amount of tracer in milliliter transferred per minute per milliliter tissue, whereas k_2 indicates a fraction of mass transferred per time unit. By solving the differential equation we get the tracer concentration over time in the target tissue:

$$C_1(t) = K_1 C_p(t) \otimes e^{-k_2 t} = K_1 \int_0^t C_p(t) e^{-k_2(t-\tau)} d\tau \tag{1.2}$$

In order to consider also different metabolites of the tracer a more complex model is used. When the tracer enters a cell it is available in a free form and can be either bound to the

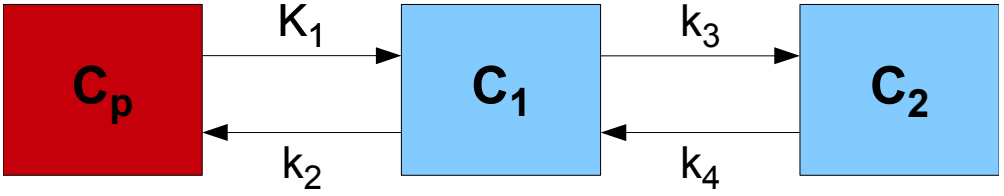

Figure 1.10: To simplify our three tissue compartment model we merge the unspecific bound tracer compartment with the free tracer compartment so we get a two tissue compartment model.

target molecule or to some other cell components which are not known in detail. These bindings lead to two new tracer concentrations C_2, for the specific bound tracer, and C_3, for the unspecific bound tracer, which are now also considered in the tracer pathways. So we get a three tissue compartment model (3TCM).

As it is extremely difficult to get all necessary transfer coefficients for the 3TCM the model is usually simplified to a two tissue compartments model (2TCM) by merging the free tracer concentration with the unspecific bound tracer concentration to the compartment C_1.

This can be done when the transfer between the unspecific bound tracer and the free tracer form is faster than the transfer between the specific bound tracer and the free form. If this is not the case the specific and unspecific bound tracers cannot be distinguished and thus the transfer coefficients for the specific bound tracer cannot be assessed.
The simplified model then yields two differential equations:

$$\frac{dC_1(t)}{dt} = K_1 C_p(t) - (k_2 + k_3)C_1(t) + k_4 C_2(t) \tag{1.3}$$

$$\frac{dC_2(t)}{dt} = k_3 C_1(t) - k_4 C_2(t) \tag{1.4}$$

1.4.2 Gamma ray emitting tracers

Tracers used in SPECT imaging are gamma ray emitting tracers (however also positron emitting tracers can be imaged), commonly used tracer isotopes are Technetium 99m and Iodine 123. Iodine is taken up by the thyroid so Iodine 123 is commonly used as a tracer to study thyroid diseases.
Technetium 99 is often combined with different molecules to image specific functions. A Technetium based tracer is for example Cardiolite where the Technetium 99m is combined with a the ligand methoxyisobutylisonitrile. This tracer is commonly used to image the myocardium. When injected intravenously it will distribute in the myocardium proportionally to the myocardial blood flow. By comparing two sets of images infarcted tissue or ischemia

can be detected. In the past one image in rest and one in stress were acquired and compared to distinguish between infarcted or ischemic tissue. Today usually at least two images under stress and two images in rest are compared to provide more accurate results.
Apart from imaging the myocardium it can also be used for imaging the parathyroid. In a first image all glands of the parathyroid are seen, a second image is taken after approximately 2 hours. On the second image abnormal glands will have a much higher concentration of Tc99m than healthy ones. It can also be used in the imaging of breast nodules, where malignant tissue often takes up the tracer in a higher concentration than in benign tissue.
Other Technetium based tracers allow for example for imaging of bones to detect bone metastasis with $^{9}9m$Tc-medronic acid, or functional brain imaging with Technetium exametazime.

1.4.3 Positron emitting tracers

In PET imaging positron emitting tracers are needed, the radioactive isotopes used include Carbon 11, Nitrogen 13, Oxygen 15 and Fluorine 18. The latter is used in the most common tracer for PET, Fluorodeoxyglucose (FDG). This tracer combines the radioactive isotope Fluorine 18 and a glucose molecule resulting in a glucose analog. As a glucose analog it allows for imaging in a lot of different regions as glucose is metabolized almost everywhere in the human body, however this makes the tracer also less specific than other tracers. Usually physicians try to detect regions with abnormal high sugar uptake in the patient, which can be an indication for cancer.

1.5 Tomography

3D visualization is not only popular in the cinema but also in medical imaging. The key to 3D imaging is tomography which basically means to image by sections or sectioning. The method of tomography was invented by Sir Godfrey Hounsfield in 1972.
In order to obtain 3D images usually a series of measurements of some physical effect is required, i.e. the attenuation of x-rays in material, the detection of gamma rays or the electronic signal generated by the change of a magnetic momentum. These measurements can be used to compute some properties of the material where the physical effect occurs or just the location of a measured radiation source.
When physical effects are completely described by their causes we have what is called a **Forward Problem**. In tomography however we want to retrieve the causes of the physical effects we measured. As this kind of computation tries to recover the source of what was measured by basically going the inverse way of the physical effect it is called the **Inverse Problem**. Mathematically it can be formulated as:

$$\underbrace{g(x)}_{effect} = \int \underbrace{k(x,y)}_{cause}\underbrace{f(y)}_{cause} dy, \tag{1.5}$$

With g being the observation of the physical effects and k and f being the parameterized causes of the physical effects.
Formulating and solving the inverse problem is basically what tomography is about. However the solving of the problem is mostly not that easy. Mathematically spoken most tomographic problems are so called ill–posed problems. A problem is ill–posed when one or more of the following criterias are not met:
- a solution exists.
- the solution is unique.
- the solution depends continuously on the data.
Unfortunately most tomographic problems do not meet all of these criterias due the discrete sampling of the observations which breaches the third criteria. In addition the observations are often incomplete, as full sets of measurements would usually take too much time to acquire, so there is more than one solution to the problem. Noise in the measurements and other errors in the detection process are also reasons which make the problem ill–posed. In some tomographic problems a solution doesn't even exist and only some kind of rough approximation to a solution can be computed.
Despite these problems tomographic imaging is extremely valuable in both medicine and industry as even the roughly approximated solutions still yield a lot of useful information without harming a patient or destroying an object.
There exist two major approaches for solving tomographic problems: filtered backprojection and iterative reconstructions. The filtered backprojection is based on the Radon transform. The Radon transform R can be considered as the projection of a function $f(x,y)$ along a line γ on to a plane vertical to that line (thus resulting in a point). This point is then the integral over the function along that line:

$$Rf(x,y) = \int_{\gamma} f(x,y)dxdy \tag{1.6}$$

A measurement of, for example, x-rays after traversing through an object is actually nothing else than a line integral of the absorption function. By applying the inverse Radon transform on the measurement the absorption along the line the x-ray passed through the object is retrieved.
In the filtered backprojection algorithm a series of measurements from different angles is used to compute the absorption along the measured lines [11]. By adding the lines we get an absorption image, which shows us the region of the highest and lowest absorptions. However

this will introduce blurring (star–like artifacts) in the reconstructed image. By applying a high pass filter (mostly a ramp filter) these artifacts can be eliminated. In the optimal case, without noise and a set of measurements with full angle coverage at every infinitesimal angle step, the reconstructed image will be an exact reconstruction.
The optimal case is however of course not possible and even being close to the optimal case is difficult. Furthermore the filtered backprojection is very sensitive to noise and missing measurements. Thus it is for many cases not the optimal way to perform a tomographic reconstruction.
Another method of reconstruction are iterative methods. The algebraic method is an example of these reconstructions [12–14]. If we consider each measurement p as a sum of contributions a to that measurement which occur in the discretized field of view V_p of the measurement we get an equation for each measurement:

$$p = \sum_{V_p} a \tag{1.7}$$

A set of n measurements then gives us a system of linear equations with the system matrix A with elements a_{ij} for each measurement i and each position j of the volume of interest. The algebraic reconstruction method is in effect an iterative solver of the system of linear equations. Starting with an initial guess, in each iteration h the algorithm approximates the solution $\vec{x_h}$ based on the solution of the previous iteration $\vec{x_{h-1}}$:

$$\vec{x_h} = \vec{x_{h-1}} - \frac{\vec{x_{h-1}} \cdot \vec{a_k} - \vec{p_k}}{\vec{a_k} \cdot \vec{a_k}} \vec{a_k} \tag{1.8}$$

with $k = h\%n$ and $\vec{a_k}$ being the contributions a on all discrete points in V_{p_k} for the measurement k.

1.6 Intra-operative functional imaging

Apart from giving information of the anatomy and the metabolism of the patient, imaging modalities also need to fit the requirements of certain tasks. Most imaging modalities were developed and are used as diagnostic tools to give the physicians the necessary information to find diseases or injuries. For this task the imaging modality should be as accurate as possible and give as much information as possible as every information might yield a necessary clue for a correct diagnosis.
Apart from these requirements diagnostic imaging should be also as little invasive as possible so it is possible to examine a patient without doing too much harm to him.

Figure 1.11: Big tomographic systems like SPECT/CT (left) and PET/MR (right) are used in diagnostics to acquire 3D images of the patient with high accuracy.

Imaging modalities that are used during surgery have completely different and more demanding requirements than diagnostic imaging. Intra operative images are also used for different tasks than diagnostic ones. During an intervention the main purpose of imaging is the guidance of the surgeon and maybe giving quick feedback of the impact of the actions of the surgeon. However in contrast to diagnostic images it is not necessary to get the same abundant amount of information with the same accuracy.
Medical imaging that can be used in surgery is still very limited and in the beginning of its developments. The main reasons for that are the limitations that come with the challenging intra–operative environment. Intra–operative imaging modalities need to be fast, flexible and accurate to be able to meet the requirements inside the operating room (OR). So far there are only very few intra operative imaging modalities, these include ultrasound, C-arm CT, nuclear probes and gamma cameras.

While in diagnostics the time to acquire the images is of almost no relevance, except for the comfort of the patient, time is a very limited resource during surgery. In surgery the body of the patient is exposed to extreme stress. Due to the incisions and the anesthesia a surgery should be performed as fast as possible. In addition also the surgeons are under an extreme stress and long waiting times to obtain new images will be more than just unsettling.
The size of the devices is also an important aspect as there is only a certain amount of space in an operating room (OR) and especially around a patient. Usually ORs are very crowded with surgeons, nurses and the anesthetist. In addition there are also several different devices used during surgery like a lung ventilator, screens for imaging, light sources, sensors... This makes it for each additional device introduced into the OR very important to fit in there in terms of space and it should be portable and flexible in its use.
A third very important constraint to intra operative imaging is the surgical workflow. Even a fast, small and flexible imaging modality is of no use if it cannot be integrated into the surgical workflow in a reasonable way. If for example the imaging technique can only be

Figure 1.12: Ultrasound probes can be used for anatomic imaging during surgery.

reasonably used under certain conditions which cannot be met at the point of time when the imaging is actually needed then it will be of no help. Acquiring images beforehand is no option in an intervention as the anatomy of the patient will be drastically changed over the course of the surgery. This also makes previously acquired diagnostic images a lot less useful.

In cancer diagnosis and therapy planning nuclear imaging like SPECT and PET are commonly used tools. However for intra–operative use they suffer from drawbacks which limit their application. The image acquisition is too time consuming and the devices are too bulky to be placed inside an OR. Hand held probes and gamma cameras are flexible enough to be used during surgery but they only provide 1D and 2D information respectively.

Freehand SPECT is a new imaging modality which was developed to overcome these shortcomings as it is specifically designed for intra–operative use [15]. Like SPECT it provides 3D functional imaging and employs gamma–ray emitting radiotracers. Freehand SPECT uses a hand held gamma–ray detecting probe with an optical tracking target attached to it. An optical tracking system provides the position and orientation of the probe which is synchronized with its readings. The combined data can then be used to compute a tomographic reconstruction of the radiotracer.

However in contrast to conventional tomographic systems Freehand SPECT has no gantry to provide a predefined acquisition geometry. Instead the probe is moved by hand and measurements are acquired at arbitrary positions. This makes it necessary that the system matrix is computed on the fly for each particular set of measurements. Hence the conventional methods to generate the system matrix are not directly applicable or have to be adapted to this situation. Furthermore the system was designed to be used during an

intervention, which makes the computation time of the system matrix a limiting factor. In order to achieve this, computationally fast models of the detection process of the probe are required to generate the system matrix.
In addition the freehand acquisitions are incomplete and the quality of the reconstruction is highly dependent on the acquisition geometry. However the latter is extremely operator dependent and acquisition geometries are not reproducible.

1.7 Thesis Outline

In this thesis models of the detection process of gamma probes are presented. The models can be used to build up a system matrix on the fly to perform Freehand SPECT reconstructions. Three different types of models are presented in the second chapter. Two analytic models, the solid angle model and the partition model and one phenomenological model, the look up table model. The effects considered by the analytic models as well as their mathematics will be described. In addition different possibilities to generate the look up table model are described.
A possible method to deal with the problems that arise from the freehand acquisition geometry is presented in the second chapter. The method uses information from 3D diagnostic images to simulate different possible scanning geometries. These simulations are used for a reconstruction and an optimization process is used to find a good acquisition geometry for the specific case.
Experiments to evaluate both the models and the optimization of acquisition geometries are described in the fourth chapter and the results are presented.
The last chapter contains a short conclusion about the work of this thesis.

Chapter 2

Modeling of detection physics

Freehand SPECT was recently developed as a new imaging modality to overcome the shortcomings of conventional nuclear imaging in intra–operative settings [16]. Freehand SPECT combines a hand–held nuclear probe with an optical tracking system to obtain its position and orientation in space synchronized with its reading. This combined data is used to perform a tomographic reconstruction of an activity distribution. With this imaging modality the accuracy and success rate of cancer surgery could be improved. Clinical studies have shown that the system can improve the sentinel lymph node biopsy procedure as a first step towards clinical applications [15, 17].

Conventional tomographic systems have a fixed pre-defined acquisition geometry based on a gantry. Typically a ring of detectors or a panel of detectors is moved on a circular trajectory around the patient, or sometimes on a trajectory fitted to the patients body contour. Inside the ring of detectors, a fixed volume of interest V is defined, which is discretized into voxels x_i. The probability a_{ij} of detector j detecting emissions from voxel i will be denoted as: $a_{ij} = P[\text{detected in } j|\text{emitted in } i]$ [7]. The measurements m_j of detector j are considered as independently distributed Poisson random variables, with the expectation:

$$E(m_j) = \sum_i x_i a_{ij}, \tag{2.1}$$

A set of measurements $m = (m_j)$ then yields a system of equations:

$$m = Ax, \tag{2.2}$$

which is solved for the activity value x_i in each voxel. Here $A = (a_{ji})$ denotes the system matrix, each entry a_{ij} representing the contribution of voxel i in measurement/detector j. To solve this system of equations most commonly a special form of iterative reconstruction is used, the Maximum Likelihood Expectation Maximization (MLEM). This solver computes

a solution which makes the measured data most likely to occur. For each iteration a solution x^h is computed for every x based on the solution of the previous iteration x^{h-1}:

$$x_l^h = \frac{x_l^{h-1}}{\sum_j a_{jl}} \sum_j \frac{a_{jl} p_j}{\sum_k x_k^{h-1} a_{jk}} \tag{2.3}$$

Here $A = (a_{ji})$ denotes the system matrix, each entry a_{ij} representing the contribution of voxel i in reading j. These contributions can be regarded as the product of different effects of the detection process. The most important factor is the detector response to a source in voxel i, other factors include, amongst others, attenuation in the patient and scattering. To solve this system of linear equations the system matrix A has to be computed. Typical methods to obtain the system matrix are analytical models of the detector response of the system [18], or measurements of a point source at the positions of all voxels of the volume of interest [19] [20] and Monte Carlo simulations of the whole system [21]. Usually the whole system matrix or at least the detector response is precomputed using these methods, however there exist several works where models were implemented to compute the system matrix on the fly to correct for attenuation and scattering [22] [23].

In Freehand SPECT however there is no fixed acquisition geometry, as the nuclear probe is moved by hand around the volume of interest. Thus the measurements are acquired at arbitrary, operator-dependent positions, necessitating that the system matrix has to be computed on the fly for each particular set of measurements. Hence the conventional methods to generate the system matrix are not directly applicable or have to be adapted to this situation. Furthermore the system was designed to be used during an intervention, which makes the computation time of the system matrix a limiting factor. In order to achieve this, computationally fast models of the detection process of the probe are required. Such models will be introduced and described in the next sections.

2.1 The detection process

To detect gamma radiation probes usually use a so called scintillating crystal [24, 25]. When a gamma ray deposits energy inside the crystal due to some physical effect the crystal emits light. Behind the crystal a photomultiplier is arranged where electrons are set free by the incident light on the photocathode at the front of the photomultiplier. The electrons are then accelerated towards a dynode in the photomultiplier where they set free additional electrons which are then accelerated towards the next dynode. At the end this avalanche of electrons hits ananode where an electrical signal can be measured with a strength that is related on the energy that was deposited in the crystal.

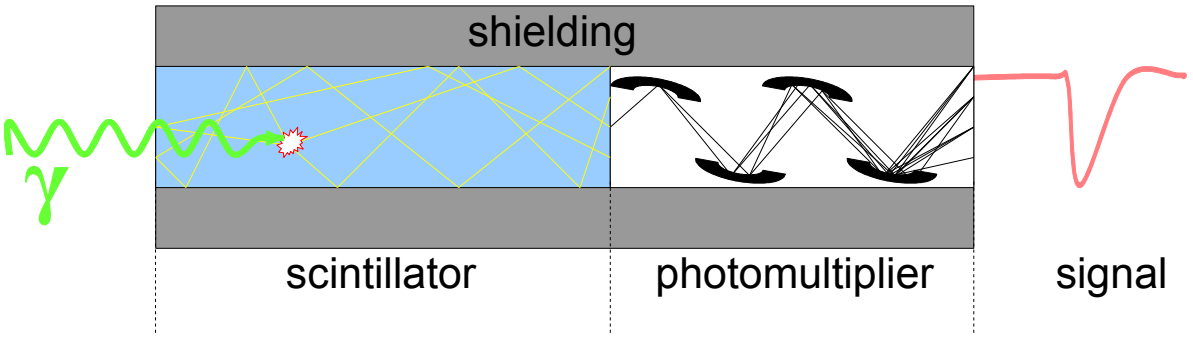

Figure 2.1: The principle of a gamma probe. When a gamma ray deposits energy in the scintillating crystal photons are emitted. The photons travel through the crystal until they hit the photocthode at the front of the photomultiplier and electrons are set free. These are accelerated towards the dynods where they set free additional electrons. On the anode at the end of the photomultiplier an electrical signal can be measured.

To model this process we need to take a look at the full path from the radioactive source to the signal and consider everything that can happen in between. With this knowledge we can then identify the gravity of every effect on the detection process and create mathematical descriptions of the effects we want to model.

2.1.1 Radioactive decay

The path of the radiation till its detection starts in the source which is a radioactive substance where the gamma rays are emitted from as the result of radioactive decay. Any radioactive substance decays and as an aftereffect it sends out radiation [26, 27]. However it is not possible to foretell when a decay occurs, there is only the half-life period ($t_{1/2}$) that is an expectation value for the time taken until there is only half of the original amount of the substance left. The amount of atoms that decays in a certain amount of time (t) can be computed with the half-life period and the known initial amount of atoms (N_0):

$$N(t) = N_0 - N_0 e^{-\frac{ln(2)}{t_{1/2}}t} \tag{2.4}$$

The radioactive decay can mathematically be described as a Poisson process. It is a counting process with no events occurring simultaneously. Furthermore the events are independent

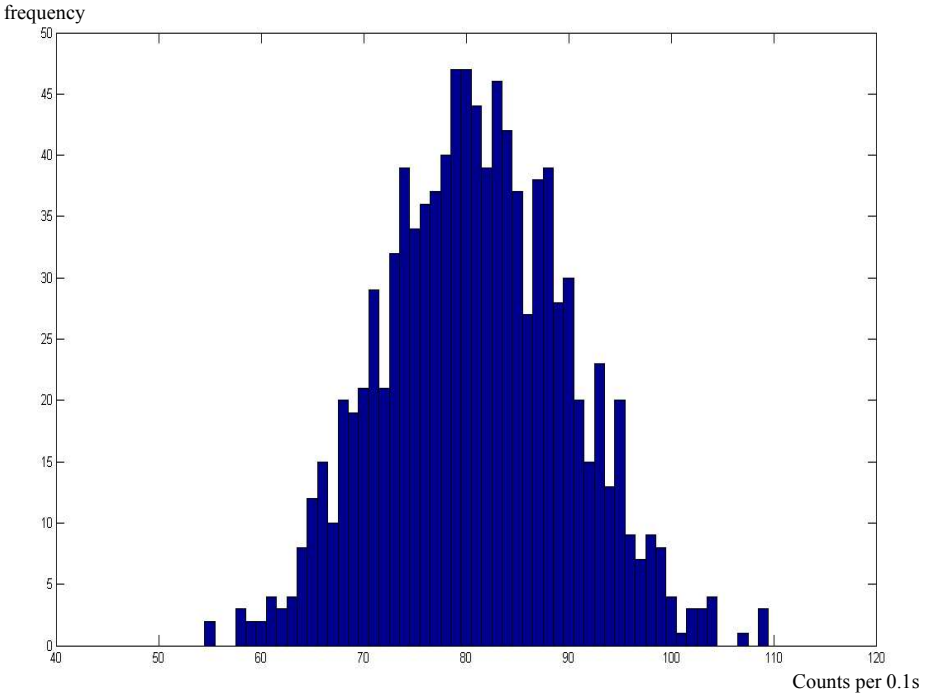

Figure 2.2: The distribution of counts from the source in a fixed configuration (constant relative position and angle between source and probe). The distribution is very close to a Poisson distribution.

from each other and the number of events in one time period is independent from the number of events that occurred before because the time for one data acquisition is short enough so that the finite number of radioactive atoms does not really influence the number of decays we get in that time (see Figure 2.2).

2.1.2 Solid angle

After the rays are emitted from the source the next thing to consider is the geometric configuration of our setting. The solid angle describes the loss of radiation due to the fact that a portion of the emitted rays simply never reaches the detector in a specific geometric configuration. I.e. a gamma ray that is emitted in the opposite direction of the probe will never reach the detector and thus cannot be detected.
The geometric attenuation is therefore a major effect that has to be considered as most of the radiation will be lost due to it.

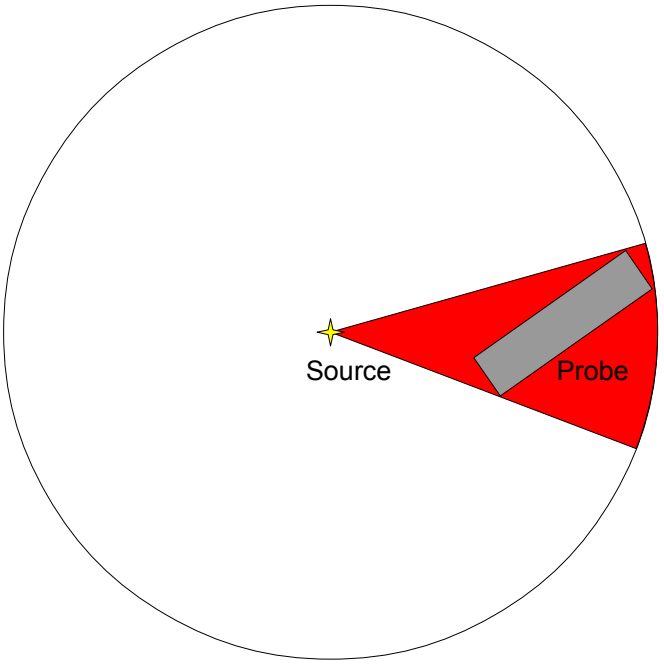

Figure 2.3: A 2D sketch of the influence of the geometric attenuation. Only rays that are emitted into the red area will reach the detector while all rays emitted in the white area are lost.

2.1.3 Photoelectric effect

On the path from the radioactive source to the detector several physical effects can occur. The photoelectric effect is one of the most important effects for gamma radiation in the energy spectrum we are interested in.
In the photoelectric effect the energy of a photon is absorbed by an electron it hits, if the energy is higher than the binding energy of the electron it is ejected from the atom [28–31]. If an electron was released from the atom an electron from an outer shell will take its position and the excess energy is emitted as a photon. If this occurs in the scintillating crystal the emitted photons can then be used to generate a signal. This effect is also important in the shielding of the probe where it is a desired effect that a gamma ray gets absorbed.
The photoelectric effect is a probabilistic effect, with the probability(p) depending on the atomic number(Z) of the material it passes through and the energy of the gamma rays(E):

$$p \propto Z^5 E^{-3.5} \tag{2.5}$$

For a photoelectric effect to occur a gamma ray needs at least the binding energy of an electron to release an electron from its atom. Electrons on a shell closer to the nucleus have higher binding energies and thus a gamma ray needs higher energies to release them. When the energy of a gamma ray is raised above such a threshold energy the probability

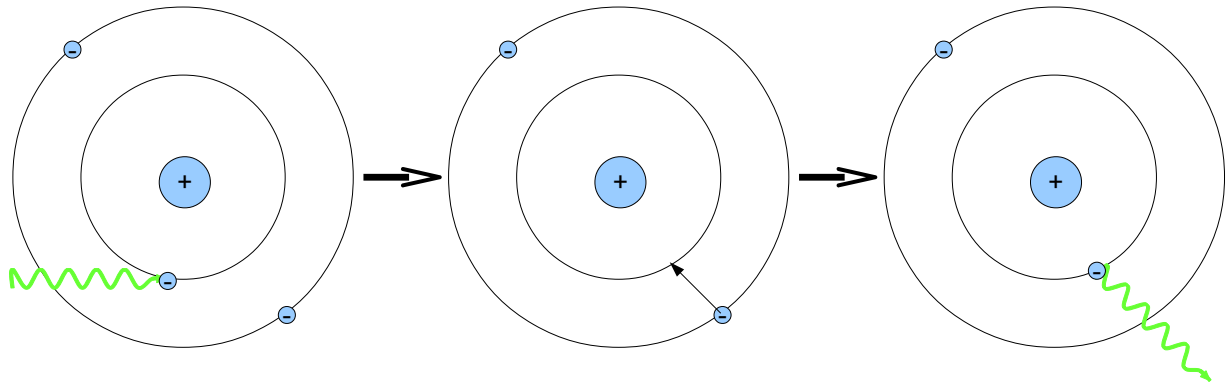

Figure 2.4: A photon hits an electron, the electron is then either emitted from its atom or is raised to an excited state. When the electron falls back to its original state photons are emitted.

for a photoelectric effect increases drastically, above that threshold the probability will then decrease again with increasing energy until the threshold for another shell of the atom is reached.

2.1.4 Compton scattering

Instead of the photoelectric effect a Compton scattering can occur when a photon hits an electron (or rarely another charged particle). The photon gets deflected and its energy is reduced and thus the wavelength is increased (Compton shift). The scattering angle (θ) depends on the change of the initial wavelength (λ) to the new wavelength (λ'):

$$\theta = acos(1 - \frac{(\lambda - \lambda')m_e c}{h}) \tag{2.6}$$

With h being the Planck constant, m_e the electron rest mass and c the speed of light.
Due to the shift in the wavelength it is an inelastic scattering although the collision itself can be regarded as an elastic one [28–30, 32].
Like the photoelectric effect the Compton scattering is a probabilistic effect that depends on the length and the material it passes through as well as on the energy of the photon. Compton scattering usually occurs with high energy radiation.

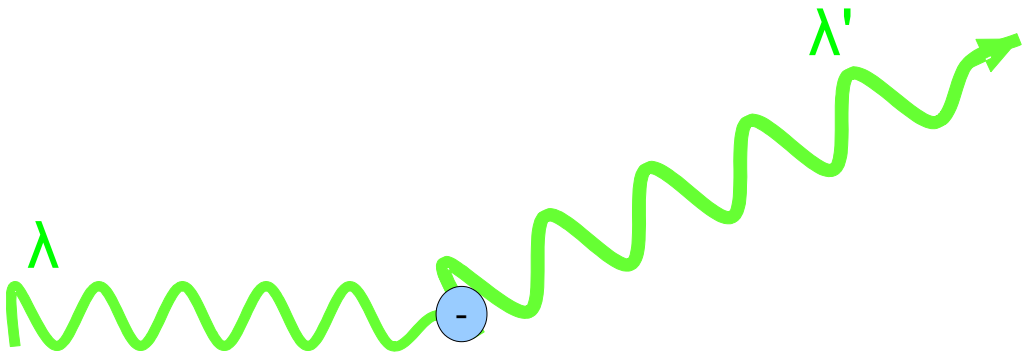

Figure 2.5: When a photon hits a charged particle the photon is deflected as a result of the collision. Its energy is reduced and thus its wavelength is increased.

2.1.5 Pair production

Pair production is a high energy phenomena where an elementary particle and its antiparticle are created. This usually happens when a photon interacts with a nucleus. However for this effect to occur the photon needs at least an energy that matches the rest mass energies of the created particles [28–30].
Thus this effect can only occur with photon energies of at least 1.022 MeV which is in an energy range that is not relevant for radiotracers.

2.1.6 Background noise

Besides the mentioned physical effects and the geometric attenuation there are other effects, like background noise, that influence the measurements. Natural radioactivity and cosmological radiation is measured by the detector [33, 34]. Radiation can also come from the detector material, e.g. from Lutetium [1]. This also contributes to this background radiation. Furthermore also light photons from outside that cross the optical shielding of the detector will cause additional counts.
To learn more about this background noise some measurements can be performed. For that purpose the probe takes measurements over a long period of time without any activity source in the room where the system should be used, so only the background noise is acquired.
This measurements give us a mean value for background noise that is independent of external parameters like orientation and position of the probe, time of the day, etc. This average noise can then be used as an approximation for a constant noise. Measurements showed that the background noise is very similar to a Poisson process (Figure 2.4).

[1] Lutetium contains commonly a certain percentage of one of its radioactive isotopes

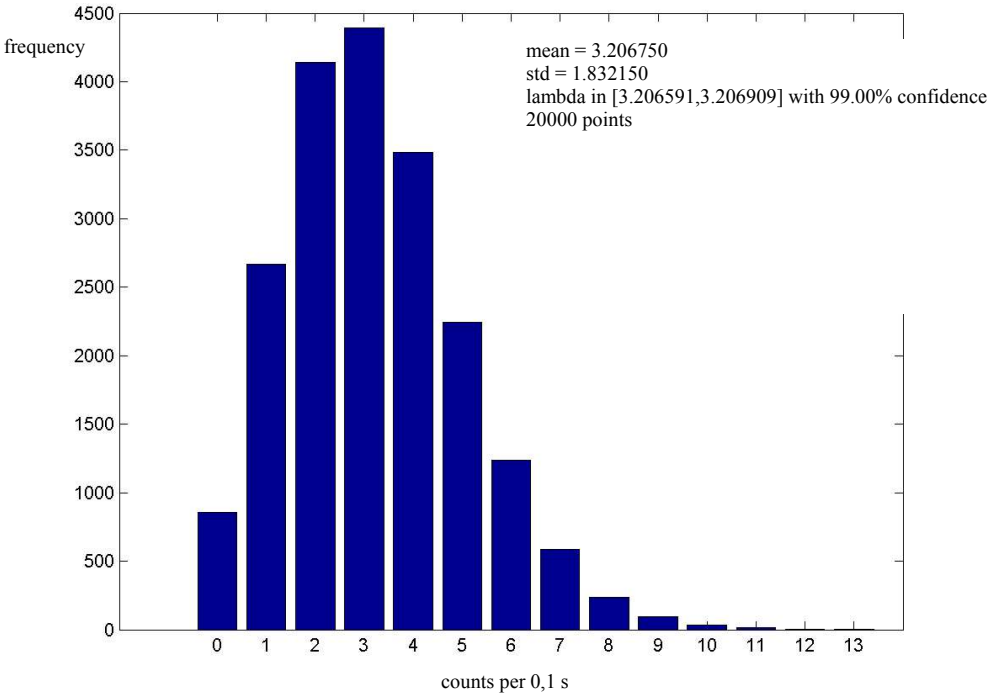

Figure 2.6: The distribution of counts from background noise. On the upper right corner some statistical values are shown. The distribution is very similar to the Poisson distribution.

The detection of background counts is clearly a counting process in the sense of statistics. No counts take place at the same time and the number of counts is independent from time. This is due to the effect that radioactive detector material like Lutetium have very high half-life times (Lutetium: $3.78 \cdot 10^{10}$ years) and background noise sources like cosmological radiation do not change considerably during an experiment.
This explains our observations and makes an additive Poisson process a good mathematical model for the background noise.

2.2 State of the art

Modeling a detection process and computing a whole system matrix is needed for tomographic imaging systems like SPECT, PET and has been done since these imaging techniques were developed. Different approaches were developed to compute the system matrix for these devices. The major techniques include Monte Carlo simulations of the whole system, analytical models of the system and approximating the system matrix with measurements acquired over a set of experiments with the target system. In this section these techniques are introduced and discussed briefly.

2.2.1 Analytical modeling

The most common way to obtain the system matrix is by deriving an analytical model to compute the number of photons that are detected by the system [22]. This is done by a series of equations which describe different physical effects in the path of the emission of one gamma ray to its detection in the detector. We define these equations in a reference frame (O, x, y, z) to the scanner with O being the center of the field of view, (O, z) the scanner axis and (O, x, y) bing the central plane of the scanner. Especially the effects of the geometry can be computed analytically. Such models are based on functions to compute the probabilities for the detection of radiation emitted by a source in the volume of interest. The geometric response of a detector to a source and the response of the collimator are the most important factors in these functions. These collimator/detector response functions ($CDRF$) can be composed from these four factors:
1) intrinsic response function
2) geometric response function
3) septal penetration response function
4) septal scatter response function

2.2.1.1 Intrinsic, septal penetration and septal scatter response

All of these effects are usually not modeled analytically, instead a set of experiments or Monte Carlo simulations are used to estimate a function that describes these effects [35]. These functions are then included in the $CDRF$ to get an analytical description of the whole system.
The intrinsic response function depends on two factors: the uncertainty in the estimation of the position in the detector system and the effects of scattering inside the crystal. The uncertainty is a result of the position estimation method used and the noise in the signal from the photo multiplier tubes. Scattering in the crystal is only a minor effect with low energy gamma rays but becomes more important with medium to high energy rays. When rays are scattered in the crystal the spread of the deposited energy in the crystal contributes to the intrinsic resolution (the full width half maximum of the intrinsic response).
The contribution of photons that penetrate through the septa of the collimator are described by the septal penetration response. Likewise the contribution of photons that are scattered in the collimator septa and still have enough energy to be subsequently detected is described by the septal scatter response. Like the intrinsic response both factors become more important the higher the energies of the rays are.

2.2.1.2 Geometric response

By far the most important factor in the $CDRF$ is the geometric response. Raytracing is a common and straight forward way to obtain the geometric response function. In raytracing the path of a ray is followed and all effects occurring along the ray are computed. However simple raytracing is extremely costly in computational terms, so usually more efficient algorithms are used. Siddon's algorithm is one of the first and most widely used algorithms for a more efficient computation of the path of a ray [36].
If we divide our volume of interest into voxels we can define the pathway of a ray in this volume by:

$$d = \sum_i \sum_j \sum_k p(i,j,k) l(i,j,k) \tag{2.7}$$

With $p(i,j,k)$ being the voxel density and $l(i,j,k)$ the length contained by that voxel. The complexity of solving this equation directly by raytracing will scale with number of voxels in the scanning volume which would make it very costly in computational terms. In order to reduce the complexity we consider three sets of planes which divide our volume into the voxels. These sets consist of equidistant parallel planes while the sets themselves are orthogonal to each other. The voxels are the intersection volumes of these planes. For simplicity let us consider the two dimensional case where our pixels are the intersection areas of orthogonal sets of equally spaced parallel lines.
Here we will now compute the intersections of the path of a ray with these lines instead of the intersections of the ray with the individual pixels. If our area consists of $N_x - 1$ times $N_y - 1$ pixels we only need to compute the intersections with $N_x + N_y$ lines, so this algorithm scales much less with the number of pixels than the direct approach of determining the intersection of the ray with each individual pixel.

Determining the intersections with the lines is a relatively easy problem. For each orthogonal set only the first intersection has to be computed while the others can be generated by recursion as the lines are spaced equally. The intersections with the pixels are a subset of the intersections with the lines as can be seen in Figure 2.5. By identifying this subset we can determine the radiological pathway.
The ray from point 1 to point 2 can be represented parameterized:

$$X(a) = X_1 + a(X_2 - X_1) \tag{2.8}$$

$$Y(a) = Y_1 + a(Y_2 - Y_1) \tag{2.9}$$

$$Z(a) = Z_1 + a(Z_2 - Z_1) \tag{2.10}$$

with a being zero at point 1 and one at point 2. When we regard a ray intersecting with our volume of interest, then we get for the first intersection point a_{min} and for the second

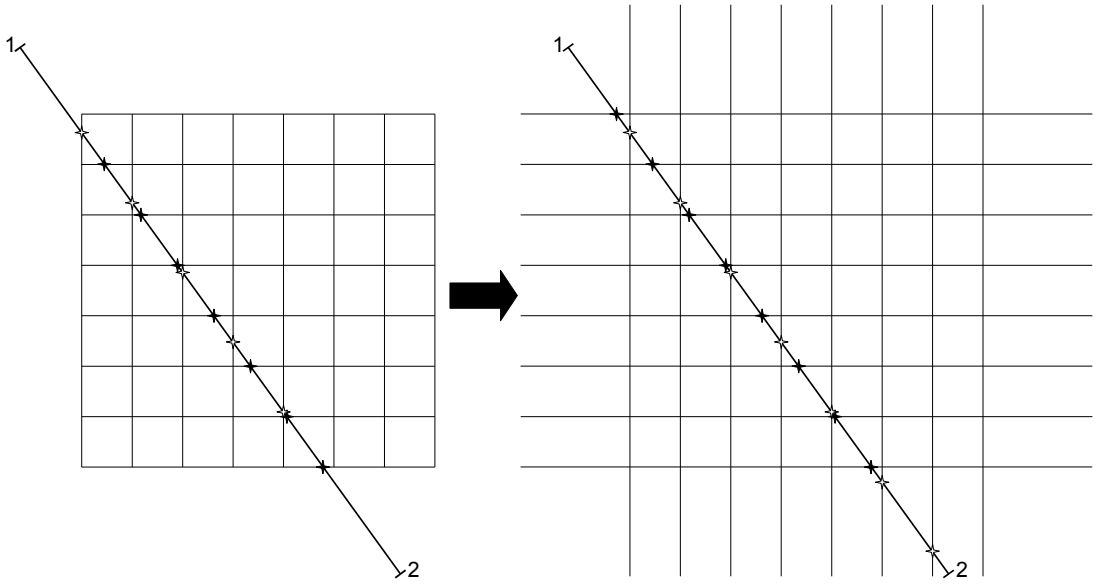

Figure 2.7: Our area of interest is divided into pixels. The pixels can be regarded as the intersection areas of two orthogonal sets of parallel lines. The intersections of a ray with the pixels of our area of interest is a subset of the intersections of the ray with all parallel lines defining the area of interest. By computing the intersections of the ray with our parallel lines we would also get all intersections of that ray with the pixels of the are of interest.

a_{max}. All of our intersections with the series of planes will then have parametric values in the range of a_{min} to a_{max}. If our volume of interest consists of $N_x - 1$ times $N_y - 1$ times $N_z - 1$ voxels we can describe our sets of planes by:

$$X_{plane}(i) = X_{plane}(1) + (i-1)dx(i = 1, ..., N_x) \tag{2.11}$$

$$Y_{plane}(j) = Y_{plane}(1) + (j-1)dy(j = 1, ..., N_y) \tag{2.12}$$

$$Z_{plane}(k) = Z_{plane}(1) + (k-1)dz(k = 1, ..., N_z) \tag{2.13}$$

With d_x, d_y and d_z being the sizes of the voxel in all dimensions and thus also the distances between the planes.
If our starting point is inside the volume of interest this point is considered as the first intersection point with the volume of interest and a_{min} is zero. Likewise if the second point is inside the volume of interest we consider that point as the second intersection point with the volume of interest and a_{max} is one. For all other cases we can get a_{min} and a_{max} by computing the intersections with the first and last plane of all three sets of planes.

Unless our ray is parallel to the x-planes the parametric values $a_x(1)$ and $a_x(N_x)$ for the intersection of the ray with first and last x-plane are given by the following expressions:

$$a_x(1) = [X_{plane}(1) - X_1]/X_2 - X_1 \tag{2.14}$$

$$a_x(N_x) = [X_{plane}(N_x) - X_1]/X_2 - X_1 \tag{2.15}$$

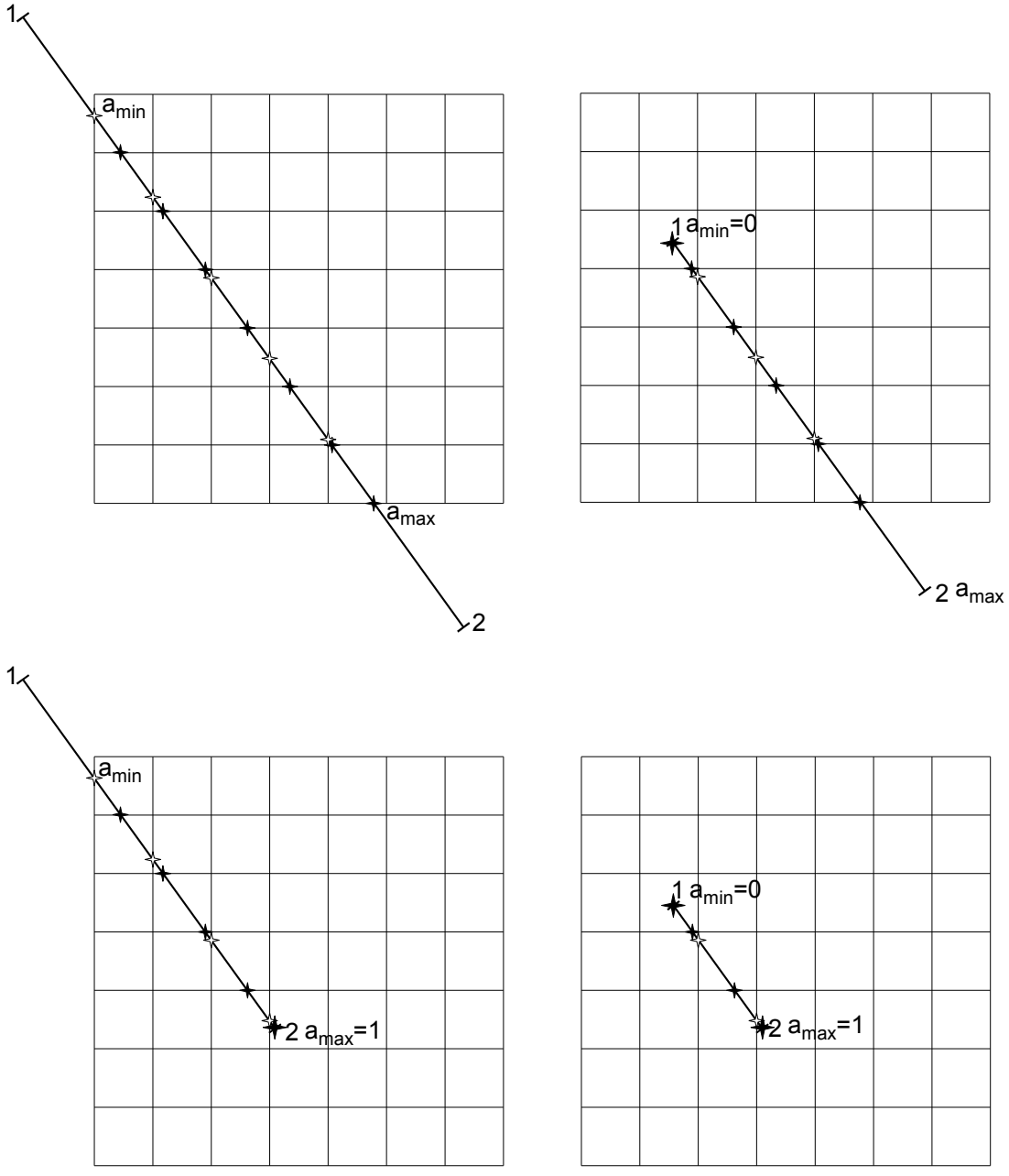

Figure 2.8: $a_(min)$ and $a_(max)$ denote the parametric values of the first intersection with the area of interest. If the starting point of the ray lies within the area of interest the parametric value a_{min} for the first intersection is zero. If the ending point of the ray is within the area of interest the parametric value a_{max} is one.

With similar expressions the parametric values for $a_y(1)$, $a_y(N_y)$, $a_z(1)$ and $a_z(N_z)$. In order for the ray to intersect with the volume of interest it needs to intersect with the first or last plane of every set. The parametric value a_{min} is thus obtained by:

$$a_{min} = max0, min[a_x(1), a_x(N_x)], min[a_y(1), a_y(N_y)], min[a_z(1), a_z(N_z)] \tag{2.16}$$

Similarly in order for the ray to leave the volume again it only needs to intersect with any first or last plane of the all sets and the parametric value a_{max} is obtained by:

$$a_{max} = min1, max[a_x(1), a_x(N_x)], max[a_y(1), a_y(N_y)], max[a_z(1), a_z(N_z)] \tag{2.17}$$

If a_{min} is greater than a_{max} there is no intersection of the ray with our volume of interest. In order to now get our intersections with the voxels of our volume of interest we only need to compute the parametric values of the intersections with all three sets of planes. We will then get three sets of parametric values, one for each set of parallel planes. Now we only need to merge these sets and sort them in advancing order. By taking the difference of two adjacent parametric values we get the fraction of the ray that passes through a particular voxel. To get the path of the ray now only the corresponding voxel indices are needed. For that we determine the indices of the first and last plane intersected by the ray in each dimension while inside the volume of interest. We get the first index i_{min} of the set of $X_{plane}(i)$ by computing the distance in x direction of the entry point of the ray to the last plane. When we divide this distance by the length of the voxels d_x we get the number of planes from the entry point to the last plane. By subtracting this number from the total number of planes in x direction we get the first plane. For the last index i_{max} we need the distance the ray passes in x direction before it leaves the volume of interest and thus also the number of planes intersected that direction. For $X_1 \leq X_2$ we get with our previous terms:

$$i_{min} = N_x[X_{plane}(N_x) - a_{min}(X_2 - X_1) - X_1]/d_x \tag{2.18}$$

$$i_{max} = 1 + [X_1 + a_{max}(X_2 - X_1) - X_{plane}(1)]/d_x \tag{2.19}$$

And conversely for $X_1 \geq X_2$

$$i_{min} = N_x[X_{plane}(N_x) - a_{max}(X_2 - X_1) - X_1]/d_x \tag{2.20}$$

$$i_{max} = 1 + [X_1 + a_{min}(X_2 - X_1) - X_{plane}(1)]/d_x \tag{2.21}$$

For the other the planes in y and z direction we get similar terms.
The set of parametric values for the intersections along the x-axis is now given as $a_* =$

$a(i_{min}, ..., a_{max})$ with:

$$a_x(i) = [X_{plane}(i) - X_1]/(X_2 - X_1) = a_x(i-1) + [d_x/(X_2 - X_1)] \tag{2.22}$$

Again with similar terms for the intersections along the y-axis and z-axis. As can be seen all intersection along one axis can be computed over a simple recursive function. With all three sets of parametric values we only need to merge and sort these in advancing order to get the set of parametric values a for the whole path of the ray. In the case that the starting point or end point is inside our volume of interest we just have to add the parametric values a_{min} and a_{max} to that set:

$$a = a_{min}, sort[merge(a_x, a_y, a_z)], a_{max} = a(0), ..., a(n) \tag{2.23}$$

with n being:

$$n = (i_{max} - imin + 1) + (j_{max} - jmin + 1) + (k_{max} - kmin + 1) + 1 \tag{2.24}$$

Two adjacent values in the set a correspond the intersection with one voxel of our volume of interest. For two parametric values $a(m-1)$ and $a(m)$, of our set of intersections a, the corresponding voxel $[i(m), j(m), k(m)]$ is the voxel containing the midpoint of the two intersections:

$$i(m) = 1 + [X_1 + a_{mid}(X_2 - X_1) - X_{plane}(1)]/d_x \tag{2.25}$$

$$j(m) = 1 + [Y_1 + a_{mid}(Y_2 - Y_1) - Y_{plane}(1)]/d_y \tag{2.26}$$

$$k(m) = 1 + [Z_1 + a_{mid}(Z_2 - Z_1) - Z_{plane}(1)]/d_z \tag{2.27}$$

where a_{mid} is given by:

$$a_{mid} = [a(m) + a(m-1)]/2 \tag{2.28}$$

For the path of our ray we now only need the length $l(m)$ it passes through that voxel, which is given by:

$$l(m) = d_{1\ 2}[a(m) - a(m-1)]\ (m = 1, ..., n) \tag{2.29}$$

with $d_{1\ 2}$ being the distance from point 1 to point 2:

$$d_{1\ 2} = \sqrt{(X_2 - X_1)^2 + (Y_2 - Y_1)^2 + (Z_2 - Z_1)^2} \tag{2.30}$$

The path of our ray is now given as:

$$\sum_{m=1}^{m=n} l(m)p[i(m), j(n), k(n)] = d_{1\ 2} \sum_{m=1}^{m=n} [a(m) - a(m-1)]p[i(m), j(m), k(m)] \tag{2.31}$$

2.2.2 Monte Carlo simulations

Monte Carlo simulations are used to solve deterministic problems by employing a probabilistic analogon. With them, complex systems can be simulated by repeated sampling of random processes. Thus the name Monte Carlo which was inspired by the casinos in Monte Carlo. If the sampling is high enough a result is obtained that represents the expected result according to the law of large numbers.
In the advent of quantum mechanics Monte Carlo simulations were first used in nuclear physics as a means to compute radiation matter interactions. The first notable use of Monte Carlo simulations was in the Manhattan Project to determine the average distance a neutron would travel through matter [37]. Since H. O. Anger used Monte Carlo simulations to compute the physical response of his new scintillation camera in the early 1960s Monte Carlo simulations have been widely used in radiation detection physics. As the processes involved are mostly random processes Monte Carlo simulations are very well suited for that kind of computation [38, 39].
For the simulation of the detection process usually a raytracing approach is used to follow the path of a particle from its emission from a source until it traveled a certain distance or lost all of its energy. In order to do this first the whole system and all intervening materials have to be modeled and placed into a geometrical context to each other so all possible interactions are considered. Then the sources are defined and placed into the defined simulation geometry. This is the simulation setup.
The use of Monte Carlo simulations in SPECT and PET was aided by the existence of general purpose code, which was developed for high energy physics and dosimetry (i.e. GEANT). These are especially used to simulate particle transportation, which is an integral part for the simulation of a SPECT or PET system. In addition the geometric and physical similarity of these tomographic devices made it easier to also develop code specifically dedicated to them.
General purpose code like GEANT has the advantage of being used by a large community and being open source. This makes it easy accessible and a lot of documentation and support can be found on the Internet. Further such code is usually more stable as a large community gets insight to the code and thus errors in the code are found more easily. It is also often maintained over longer spans of time and regular releases, supporting the newest technology, are often available. On the other hand, however, in order to be general purpose code it needs to have much more functionality than one would need. This makes it harder to understand and use, as one has to first find out which parts of the code he needs for his simulation. Also it usually requires a lot more programming in order to get a specific simulation setup. This is also a source for errors, so the simulation has to be carefully evaluated. Dedicated code for SPECT and PET simulations fit perfectly for the simulation of these devices and setting up a simulation for these devices is relatively easy. However dedicated

code lacks flexibility, as it was usually developed with a specific setup in mind. It is also as well maintained and documented as general purpose code as the community using the code is not big enough.
For the accuracy it is important which particles and components are simulated and how they are simulated. Validation of the code and extensive testing is also important to ensure all parts of simulation work as intended and that there are no bugs which influence the accuracy.

2.2.2.1 GEANT4

GEANT4 is the newest version of the GEANT (**Ge**ometry **an**d **T**racking) series of Monte Carlo simulation frameworks for particle interactions [40]. It was developed by CERN and covers a large range of particles from short to long living in wide range of energies (from 250 eV to 1 PeV). For these particles all relevant processes from optical, electromagnetic to hardonic are implemented. The framework was also extensively tested and validated with experimental results and reference data.

2.2.2.2 GATE

One of the most widespread simulation framework for Monte Carlo simulations in nuclear medicine is GATE [41, 42]. GATE is based on the Geant4 framework which was developed in CERN to simulate the effects of particles passing through different materials. An additional abstraction layer was designed specifically for simulations of emission tomography. That way it combines the advantages of well tested and documented general purpose code while being as easy to use as dedicated code.
To set up a simulation in GATE an interactive scripting language is used. Commands can also be saved in macros which can be executed at the start or during a simulation. With the scripting language the geometry, sources, detectors are defined. In addition different kind of movements can be executed. With the time management offered by GATE the user can also control certain events during the simulation. In addition if the basic functions of GATE are not enough the user can also define new classes to introduce new functions to GATE. This requires however more knowledge about the implementation of GATE.
To control the output of a simulation detectors have to be defined. GATE offers two types of detectors. These are just bound as a property to a certain geometric element of the simulation. The so called crystalSD which is used to define the detectors of the device one wants to simulate, but it can also be attached to any other geometric element. During the simulation all interactions that take place in these elements are recorded. The other detector

type is the phantomSD. It is used to record information about Compton and Rayleigh scattering. This can be used to estimate if detected photons were scattered or not.

2.2.3 Direct measurements

The system matrix can also be acquired from a set of measurements of a point source [20]. This is the most straight forward method for acquiring the system matrix. The set of measurements is acquired by using a positioning system to place the point source at different locations within the reconstruction volume. At each position measurements are taken for an amount of time sufficient to get a statistically stable set of measurements. Ideally these measurements cover all voxels of the volume, in that case the measurements can be directly used as the system matrix. However as the desired volume and voxel sizes are changed from reconstruction to reconstruction the system matrix is usually computed for the desired reconstruction volume from a set of measurements via interpolation.
As the acquisitions needed for this approach usually take several days or even weeks and require an accurate positioning system it is not commonly used. Especially as the acquisition process itself is very sensitive to disruptions, i.e. tremors, it is very difficult to get a valid set of measurements. For small animal SPECT and PET systems this approach an easy way to obtain the system matrix as the smaller volume of interest allows for a faster acquisition of the whole system matrix.
A faster approach to obtain the system matrix by direct measurements is by taking the measurements with only one or a few detector elements. The whole system matrix is then obtained by extrapolating the results to the whole detector array.
Direct measurements are also used to improve the accuracy of analytic models. This is done by using the measurements to acquire parts of the system matrix which are only difficult to obtain by analytical modeling, like the detector response. Another approach would be by fitting the resulting function of the analytic model to the results of the measurements [19].

2.2.4 Methods in comparison

All of the above mentioned methods are used today in practice and each of the methods produces good reconstructions which are quite similar in comparison. Advantages and disadvantages of the different methods are mainly found in the generation of the system matrix. While an analytical model is the fastest method to generate the system matrix and also seems to handle projection noise better [43] it is very difficult to model the effects in the detector and the collimator. Thus usually these effects are obtained by using Monte Carlo simulations.
Measurements can be either used on its own to generate a system matrix or to generate the

parts of the system matrix which are difficult to model. This is the most straightforward method, however the acquisition is quite tedious, requires additional hardware and can be very time consuming. In addition the short half life of many commonly used tracers make this approach even more difficult.

With more computing power and tools available Monte Carlo simulations grew more attractive in the last years [44]. Monte Carlo simulations are a good alternative to generate a system matrix as with tools like GATE setting up a simulation is relatively easy. The simulation then takes care of all necessary effects by itself and is well fitted to deal with the statistical effects in the process of detecting radiation. However an extensive simulation will take a lot of computing power and time.

Chapter 3

Models of detection physics for Freehand SPECT

3.1 Solid angle model

In the following section an overview of the solid angle model will be given, and the effects that have been taken into account will be described.
As a first approach in this model, the measured activity (p) of a given point source in space of the probe is considered as a product of certain factors (a_i) with the activity (x). This can be written as:

$$p = \prod a_i \cdot x. \tag{3.1}$$

As the rays of a point source of activity are spread equally in space the percentage of rays that reach a certain area (A) can be measured over the solid angle (Ω_A) subtended by the area referred to the source.
The front of the detector is such an area and so the use of the solid angle of the sensor's front is an easy way to get an appraisal of the geometric attenuation, assuming the probe is otherwise perfectly shielded. For most probes the area is a circle with radius r, so if the plane of the circle is perpendicular to the vector from the source to the center of the said circle, the percentage of rays crossing the detector is calculated by the ratio of the area integral over the infinitesimal solid angle elements of the circle

$$\Omega_A = \int_A d\Omega = \int_A \frac{d \cdot r \cdot dr \cdot d\vartheta}{2\sqrt{r^2 + d^2}^3} \tag{3.2}$$

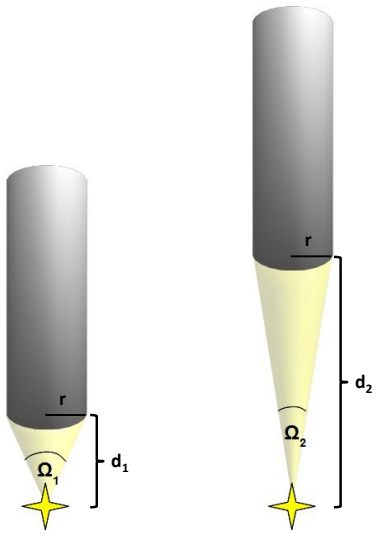

Figure 3.1: The solid angles Ω_1, Ω_2 subtended by the detector A with radius r referred to the source for two different distances d_1, d_2.

to 4π (Figure 3.1). Here r and d are defined in Figure 3.1 and ϑ is the polar angle in the plane of the circle.
For the percentage we get:

$$\frac{\Omega_A}{4\pi} = \frac{1}{2} \cdot \left(1 - \frac{1}{\sqrt{\frac{r^2}{d^2} + 1}}\right). \tag{3.3}$$

To a get better approximation of the geometric attenuation we somehow have to take into account that the front of the detector is not always orthogonal to our source but has a certain inclination angle (α). The use of the cosines of this angle as further multiplicative correction yields a better approximation (Figure 3.2).

So far we regarded our detector somehow just as an area, but as the detector is a three dimensional object we can improve our model further by considering this fact. Every ray that reaches the detector will go through the detector some length, this is the length where an interaction (a detection) may happen (Figure 3.3). Given that, it will be further referred to as length for interactions (l_i).
The longer it is the better is the chance of the ray being detected. To consider this for a given angle α the length for interactions is estimated and a factor v, that considers the ratio between the length for interactions and the total length of the detector l, is appended to

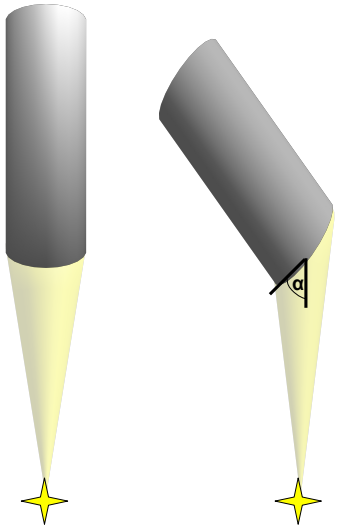

Figure 3.2: The solid angle with and without an inclination angle α. For $\alpha > \frac{\pi}{2}$ as a first approach we shall consider that no activity will be detected, as the detector is shielded from the sides.

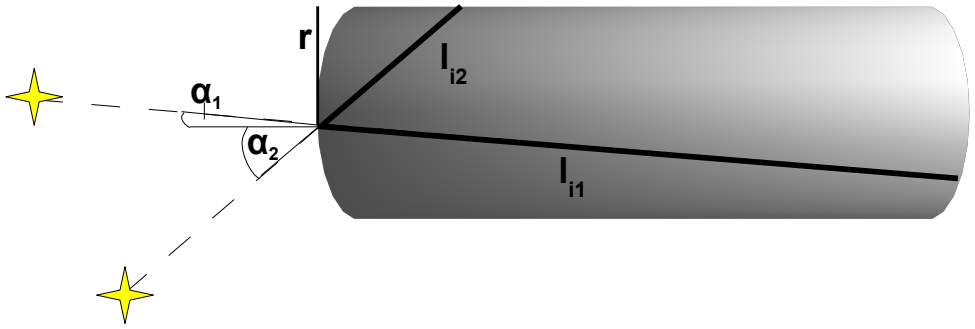

Figure 3.3: The lengths of interaction l_i for two different sources in a detector with radius r and length l. Here only rays through the middle of the face of the detector are shown as the shielding is regarded as perfect.

the previous geometric attenuation. In a first approach

$$v(\alpha, r, l) = \begin{cases} \frac{1}{\cos(\alpha)} & \text{for } \alpha \leq \arctan(\frac{r}{l}) \\ \frac{r}{l \cdot \sin(\alpha)} & \text{for } \alpha > \arctan(\frac{r}{l}) \end{cases} \tag{3.4}$$

is used.

As a summary the geometric attenuation can be written as

$$p = \underbrace{\frac{1}{2} \cdot \left(1 - \frac{1}{\sqrt{\frac{r^2}{d^2} + 1}}\right)}_{\text{solid angle}} \cdot \underbrace{\cos(\alpha)}_{\text{angle of deflection}} \cdot \underbrace{v(\alpha, r, d)}_{\text{length for interactions}} . \tag{3.5}$$

3.1.1 Detection of gamma rays

To complete our model we need to consider the detection process further. Not all rays that reach the detector are really detected. This can be represented by an additional factor that also takes care about some other effects that have not been considered yet and include further effects implicitly. A ray is only detected if an amount of energy above the energy threshold of the probe (fixed by the user) is deposited in the scintillator crystal. This may happen due to a photoelectric absorption or a Compton scattering process. Both processes are statistical as there is only a chance for a ray to cause such an interaction.
For every ray that comes from the same direction we have the same chance, given for example by length for interactions referred to an ideal 100% absorption probability length, of being detected, so we can regard any of these rays as a random experiment. Then during a detection we have a certain number of random "experiments" with the same chance and this can be modeled as a binomial process.
In a first approach only a constant sensitivity is used and for a second case the factor v discussed in the last section is used.

3.2 Partition model

In this section the idea behind the partition model will be described. Moreover, all new effects that have been included in this model are explained, as well as, the way they are implemented.
The partition model works quite similar to the solid angle model. It uses, however, more information about the geometry of the probe to be more accurate when dealing with the geometric attenuation and the process of detection. Furthermore, the shielding and the effect of Compton scattering are modeled here too.

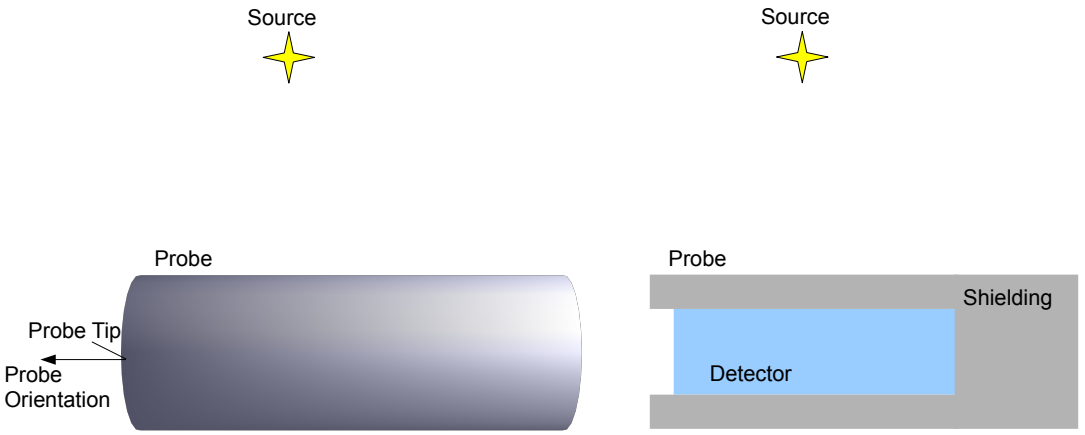

Figure 3.4: We consider only the profile slice of the probe at the intersection with the plane defined by the source position, the probe tip and the probe orientation vector. With the four rays to the corners of the detector we compute the geometric attenuation by dividing the angle β between the two outermost rays by 2π. Further we compute the length l_i these rays traverse through the detector. These are used to determine the probability of an interaction in the detector.

3.2.1 Effects of the geometry

In the partition model the geometric attenuation is determined in a similar way as in the solid angle model. However as the assumption of the perfect shielding is dropped not only the front of the detector is considered to compute the geometric attenuation. Instead the partition model takes into account the whole detector for the computation of the geometric attenuation.

Due to symmetry we can reduce our computations to a profile slice through the probe. The considered slice lies on the plane defined by the source position, the tip of the probe and the directional vector of the probe orientation (Figure 3.4). In this slice we consider the four rays which go through the corners of the detector (Figure 3.5). To compute the geometric attenuation we take the angle β between the two outermost rays and divide it by 2π.

$$a_{geom} = \frac{\beta}{2\pi} \tag{3.6}$$

3.2.2 Detection

In order to be able to compute the effects of the shielding and the absorption in the detector, we need to calculate the mean lengths that rays traverse through the shielding and the detector. We refer to these lengths as the lengths of interaction (l_i). The computation of these lengths depend on their position relative to the probe. Therefore we divide the space

around the probe into partitions (P1-P4 for the lengths through the crystal and P1-P5 for the lengths through the shielding see Figure 3.5 and Figure 3.6) which determine the way the lengths are computed. Due to symmetry we can reduce our computations again to the 2D slice of the probe.

When a gamma ray interacts with the material it is passing through several effects can take place depending on the energy of the ray and the nature of the material. The most important physical effect is photoelectric effect as it is the effect with the highest probability in our scenario and it is the effect that usually leads to the detection of a gamma ray. The mean length for interactions in the scintillation crystal is used to compute the probability for a photoelectric effect.

Four exemplary rays are casted through the corners of the detector and the length for interactions l_i' along these rays are computed.

Using the length for interactions, we can compute the probability p of an interaction with the detector along that ray:

$$p = 1 - e^{\mu l_i} \text{ with } \mu \text{ being a material specific coefficient.} \tag{3.7}$$

To obtain the mean probability of an interaction we compute the probabilities between every two adjacent rays by integrating over the probability function for an interaction with the two rays as boundaries and dividing it by the difference of the length for interactions of both rays. We then compute the mean probability $\overline{p_i}$ of an interaction within the region between two neighboring rays by integrating over the probability function for an interaction with the two rays as boundaries and dividing it by the difference of the length for interactions of both rays:

$$\overline{p_i} = \frac{\int_{l_{in}}^{l_{in+1}} \left[1 - e^{\mu l_i}\right] dl_i}{|l_{in} - l_{in+1}|} = \frac{1 - \left|e^{\mu l_{in+1}} - e^{\mu l_{in}}\right|}{|l_{in} - l_{in+1}|}. \tag{3.8}$$

By weighting these probabilities with the angle β_i between these rays and dividing them by the total angle between the two outer rays β, we get the mean probability for an interaction in the detector $\overline{p_d}$ with the source on that specific position relative to the probe:

$$\overline{p_d} = \sum_i \overline{p_i} \frac{\beta_i}{\beta}. \tag{3.9}$$

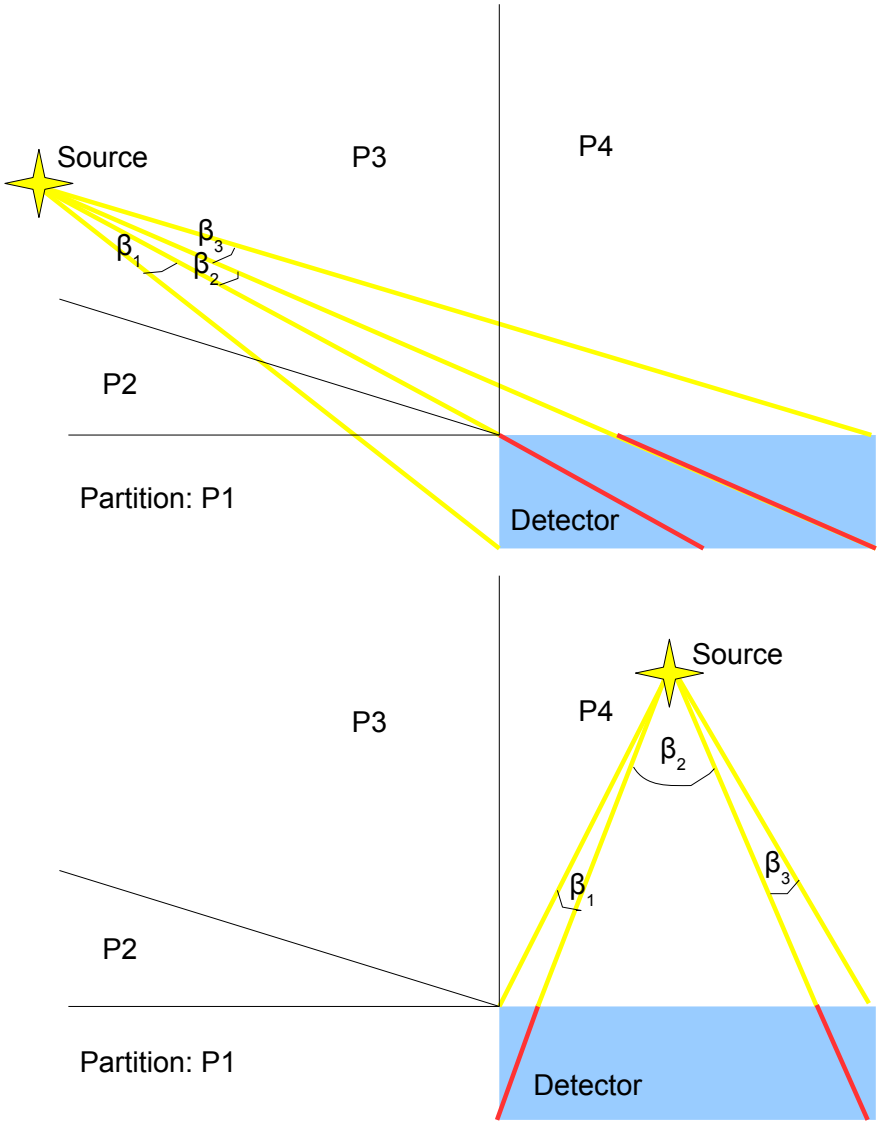

Figure 3.5: Four exemplary rays are casted to the corners of the detector and the lengths of interaction l_i along these rays are computed. Using these lengths the mean probability of an interaction in the detector is computed. The computation of the of the lengths of interaction depend on the relative position of the source to the probe. The area around the probe is divided into partitions (P1, P2, P3,P4) in each partition the calculation of the length for interactions is done in a different way.

3.2.3 Shielding

3.2.3.1 Photoelectric effect

A gamma probe is used to pinpoint radioactive sources, so only rays that originate in front of the probe should be detected. This is achieved by a shielding of the detector which is only recessed at the front of the probe to prevent rays from reaching the detector from other directions than the front.
To be able to shield the detector from rays the shielding needs to be made of a material with a very high cross section for the used radiation, for example lead or tungsten. The rays will be absorbed by the shielding only with a certain probability that depends again on the length for interactions. But this time the length for interactions that rays take through the shielding (l_i) is considered. Other factors are the material of the shielding and the energy of the rays (resulting in an absorption coefficient μ_s).

Given this there is a certain probability p_s of rays that will be absorbed in the shielding. This probability is calculated similar to the probability for a photoelectric absorption in the detector:

$$\overline{p_i} = \frac{\int_{l_{in}}^{l_{in+1}} \left[1 - e^{\mu l_i}\right] dl_i}{|l_{in} - l_{in+1}|} = \frac{1 - \left|e^{\mu l_{in+1}} - e^{\mu l_{in}}\right|}{|l_{in} - l_{in+1}|}. \tag{3.10}$$

$$\overline{p_s} = \sum_i \overline{p_i} \frac{\beta_i}{\beta}. \tag{3.11}$$

3.2.3.2 Compton scattering

Gamma rays are not always absorbed in the material by a photoelectric effect. Depending on the energy and the material the rays pass through, they have also a probability p_c to be scattered by a Compton effect. This is again computed in the same way as the absorption in the detector or shielding using a material coefficient τ similar to the absorption coefficient μ. In the case of scattering the ray is only deflected by a certain angle and has its energy reduced. The deflection angle (θ) and the final energy (E') depend on each other as described by the formula [8]:

$$E' = \frac{E_0}{1 + \frac{E_0}{m \cdot c^2} \cdot (1 - cos\theta)} \tag{3.12}$$

As some of these scattered rays may still be detected, they have to be taken into account for an accurate modeling of the detection process. Especially for high energy probes this

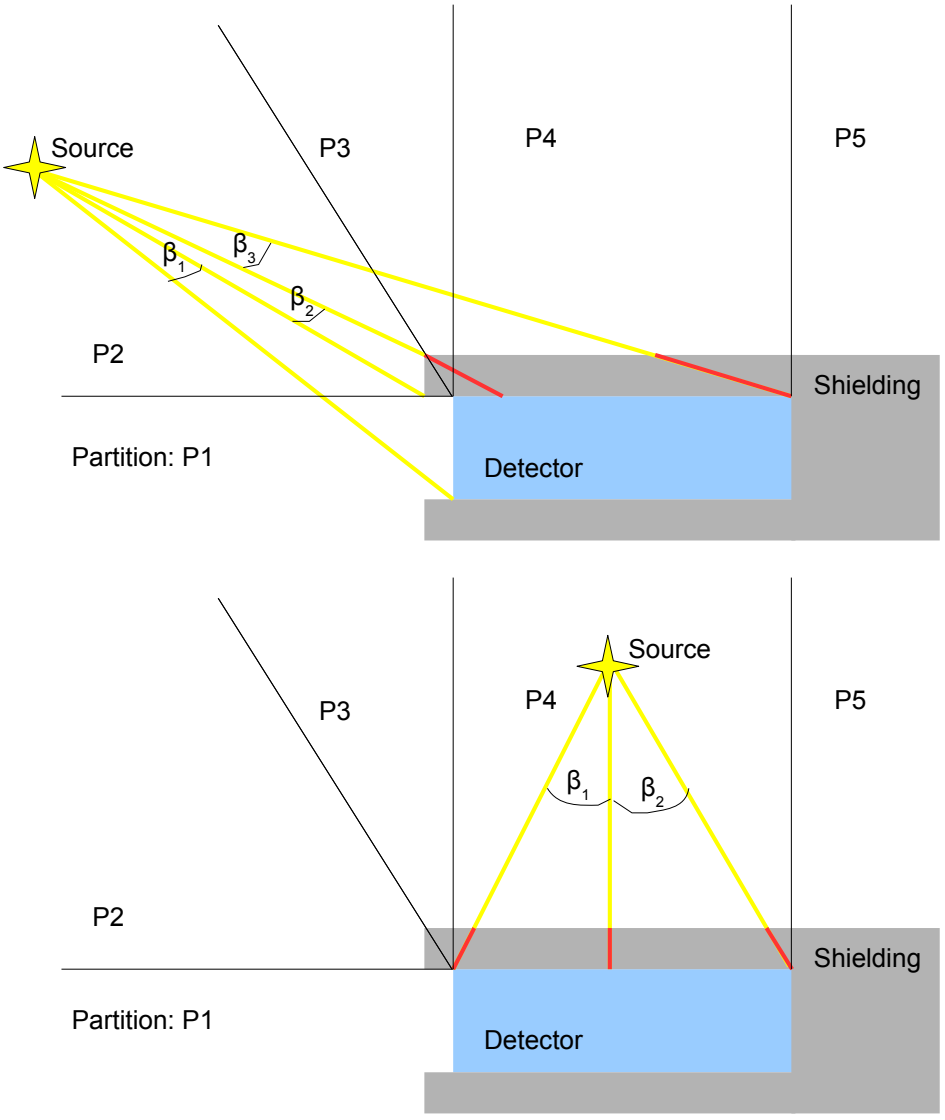

Figure 3.6: Exemplary rays are casted to the corners of the shielding and the lengths of interaction l_i along these rays are computed. Using these lengths the mean probability of an absorption in the shielding is computed. The computation of the of the lengths of interaction depend on the relative position of the source to the probe. The area around the probe is divided again into partitions (note that these are different from the partitions used for the detector) in each partition the calculation of the length for interactions is done in a different way.

effect becomes very important. In tungsten (W), which is the material of the shielding for most used probes, more than half of the interactions that occur with gamma rays that have an energy of 511 keV are Compton scattering.
To avoid the detection of scattered gamma rays or rays from other sources the probe has an incorporated energy threshold in order to filter out lower energy γ-rays. Since the energy of the detected rays cannot be determined exactly due to technical constraints the threshold is usually a rough energy window. For high energy gamma probes that should detect annihilation gamma rays with 511keV the threshold is slightly below 511keV [8] the threshold energy also depends on the energy resolution of the probe.
In practice this means that only Compton scattered rays that still have an energy above this threshold need to be taken into account. The Klein-Nishina formula, gives the probability $p_c(E_0, \theta)$ of a photon being scattered in a certain angle θ given an initial energy E_0 [8].

$$p_c(E_0, \theta) = \frac{1}{1 + \frac{E_0}{m \cdot c^2} \cdot (1 - cos(\theta))} \tag{3.13}$$

The probability $p_{c'}$ for a ray to have an energy E_t above the threshold after a Compton scattering can be calculated by determining thus the angle for E_t from equation 2.6 and then integrating $p_c(E_0, \theta)$ from 0° to that angle. These rays are then treated as described in the section about the detection process but the absorption coefficient (μ') is taken for energies that are approximated as the mean energy of the scattered rays.

3.2.4 Summary

In order to compute now the total percentage of detected rays we need to combine the different effects for the detection process. For that we first compute the probability of an unscattered ray reaching the detector by adding taking the inverse probability of the sum of the probabilities for an absorption and a scattering in the shielding. This is then multiplied with the probability for a photoelectric absorption in the detector.
In addition scattered rays with an energy above the energy threshold are considered. For that we take the probability of a ray being scattered an still having enough energy to be detected $p_{c'}$ and we multiply it with the probability of a photoelectric absorption $p_{d'}$ with the lower mean energy of these rays.
These two probabilities are then added and multiplied with the geometric attenuation:

$$a = \frac{\beta}{2\pi}((1 - (\overline{p_s} + \overline{p_c}))\overline{p_d} + \overline{p_{c'} p_{d'}}). \tag{3.14}$$

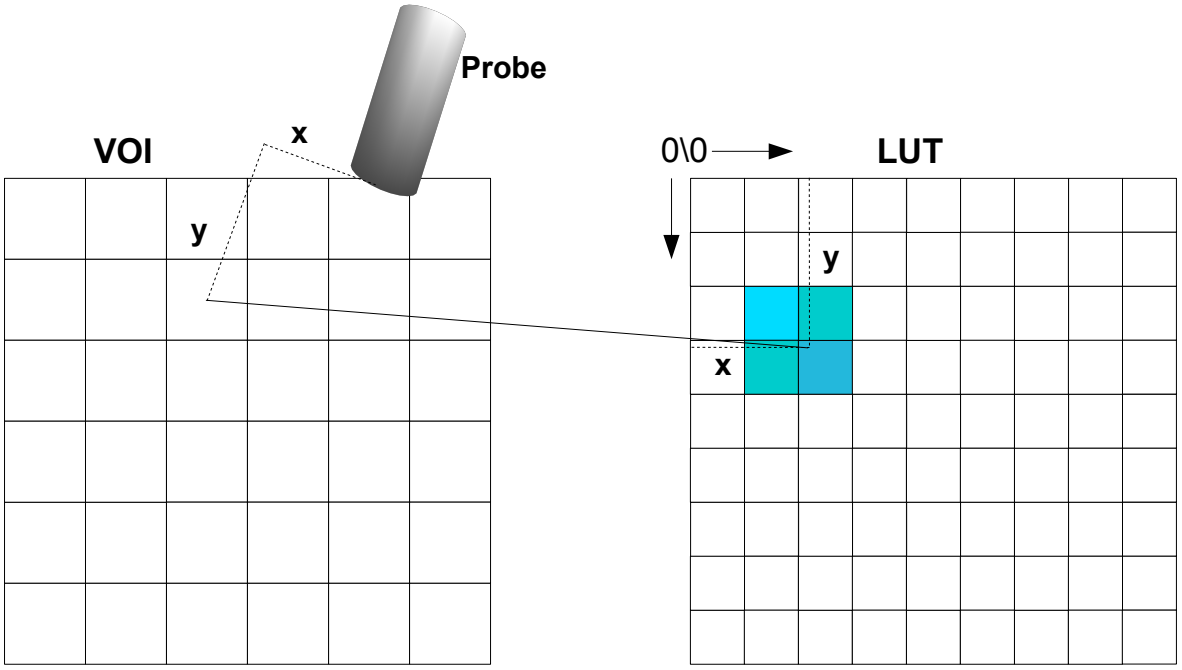

Figure 3.7: To obtain the entry of the system matrix for a certain voxel and probe position we compute the relative position of the voxel to the probe. This position is then used to get the closest entries of the look up table. The entry of the system matrix is then computed by interpolating between these look up table entries.

3.3 Look up table

Instead of analytical models we can also use a look up table of interpolated data acquired as measurements or Monte Carlo simulations. To get the contribution of a voxel to the reading we compute the relative position of the voxel to the probe. From the look up table we then take the closest entries corresponding to that relative position (Figure 3.7). By interpolating between these entries we obtain the contribution.

The entries of the look up table can either be constructed from real measurements of the used probe, similar to the generation of the system matrix in SPECT using point source measurements, or by simulations. We can measure an entry directly by placing a small source with a known activity in the respective position. With the probe we then get the amount of activity we can measure from that position, which is our entry for the look up table. By doing this for all voxels of our desired volume of interest with all probe positions we would get the system matrix. However as the acquisition geometry is not known we cannot measure the system matrix directly beforehand. Acquiring all possible system matrices beforehand is also not possible because there is an infinite number of possible probe positions and thus an infinite number of possible system matrices.

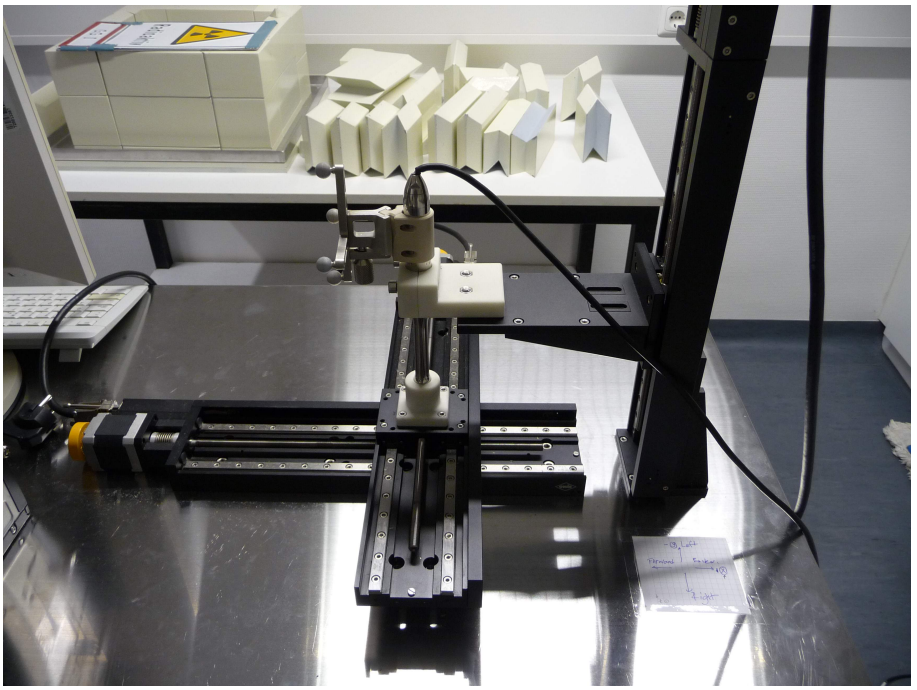

Figure 3.8: A three axis step motor device was used to acquire a look up table of measurements from a Tc99m source.

Instead we take measurements of a point source at all positions within a volume around the probe with a certain accuracy. This gives us then a look up table of measurements for different relative positions between the probe and a source.
To acquire the measurements with the probe, a step motor device with three axes was used to move a small source of Tc99m (2 MBq) to different positions with respect to the probe (Figure 3.8). The measurements of all those positions were then saved in a look up table. Alternatively the other proposed analytical models can be used to compute the look up table entries at the respective positions, or a more sophisticated simulation framework like GATE [41] can be used.

3.4 Experiments and results

3.4.1 Models in Comparison

As a first evaluation of the models we can compare their behavior with each other. The comparison shows that in general they behave similar, although the impact of the vertical distance between the probe and a source is stronger with solid angle model than with the other models. Another difference between the solid angle model and the other models can be found when we look at the behavior along the horizontal distance. There the maximum is at zero for the solid angle model while for the other models the maximum is slightly shifted.

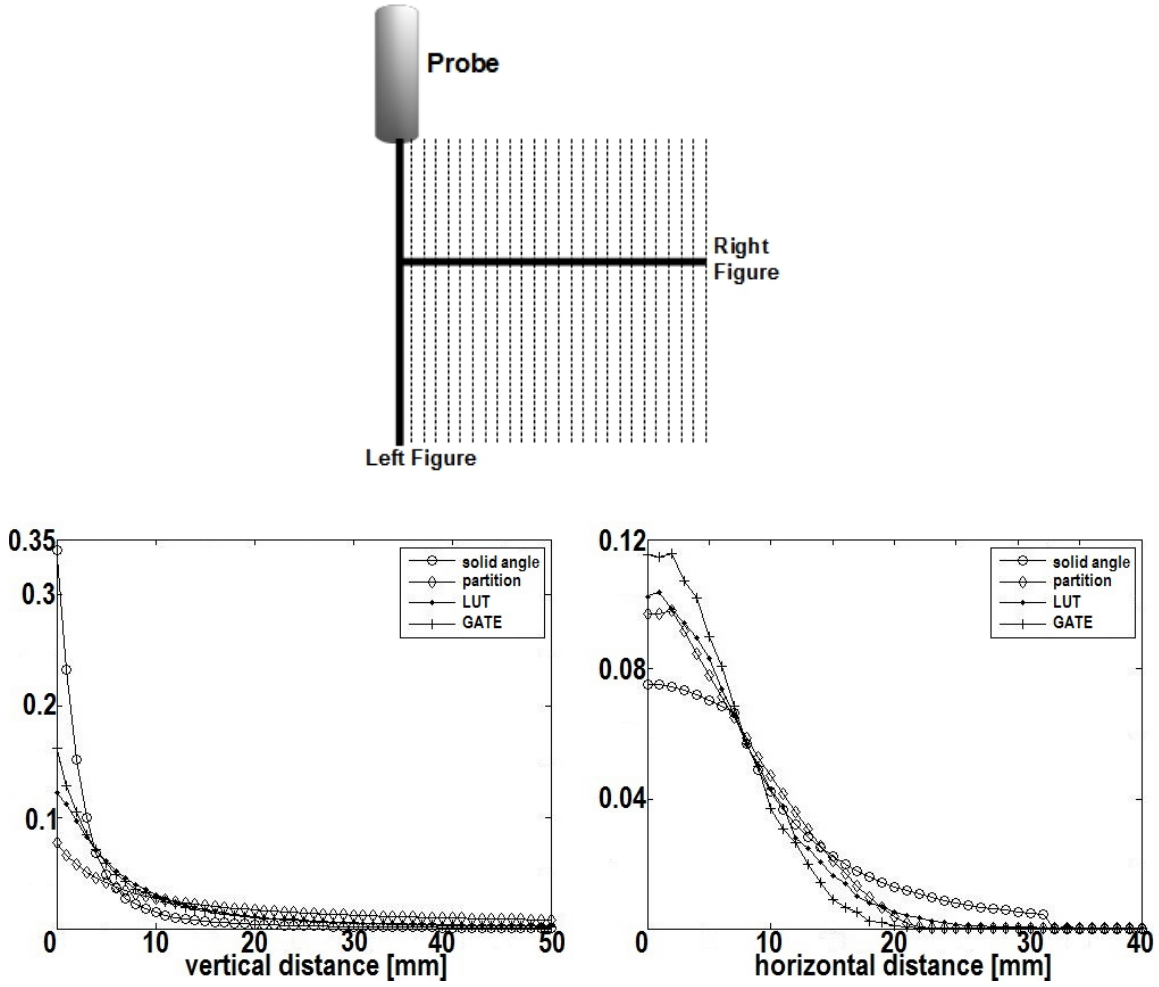

Figure 3.9: Plots of the influence of the vertical and horizontal distance of a source to the relative count rate computed with the solid angle model (circle), the partition model (diamond), the look up table (dot) and measurements generated with Gate (plus). The y-axis represents the response of the model and the x-axis represents the (left) vertical distance in mm (at a horizontal distance of 0) and the (right) horizontal distance in mm (at a vertical distance of 20mm) as shown in figure (a).

This is a result of the design of the shielding of the probe which is taken into account in the latter models.

One would expect that the look up tables generated from real measurements and GATE would have the most similar curves, which is the case for the vertical distance but not for the horizontal. There are several sources for errors which could be responsible for the different behavior. For the GATE simulations a point source was used, while for the real measurements the source had of course certain dimensions, this is probably the main reason for the different behavior in the horizontal distance. Another source of error is that in Gate we have a perfect setting where especially the position of the source is exactly defined. For the real measurements however the exact positioning is extremely difficult and thus also a source for errors.

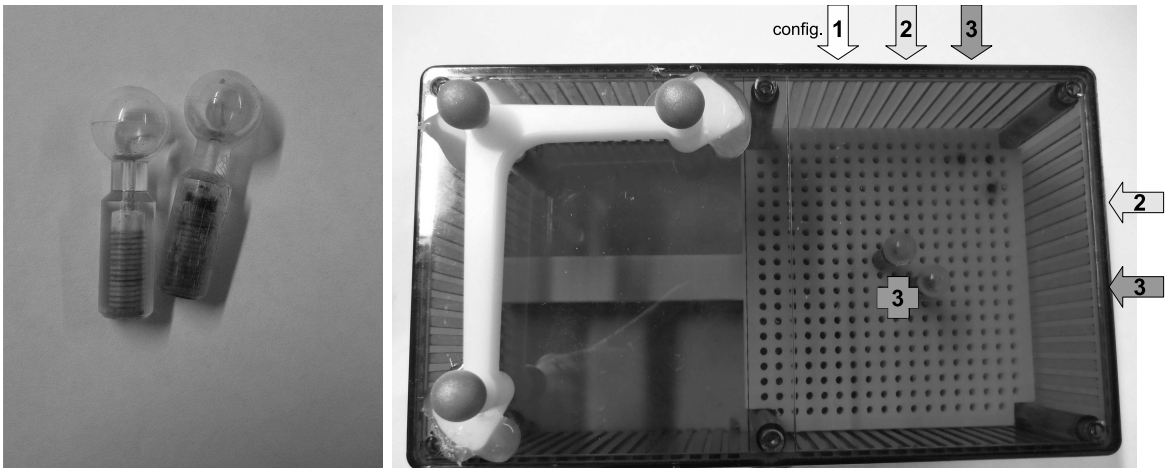

(a) (b)

Figure 3.10: The phantom consists of a box where hollow spheres (a) can be placed in different configurations. (b) Several datasets were acquired from the phantom in a first set of experiments. In each dataset different numbers of sides of the phantom were covered in the scans. The scanning configurations are indicated by the arrows (here config. 1-3 are shown, additional sides were covered in further scans).

3.4.2 Experiments

For an evaluation of the models two sets of phantom experiments were conducted. The phantom was designed to reflect the sentinel lymph node procedure. It consists of a box with approximately the size of the volume of interest in procedure. Hollow spheres can be placed at different positions inside the box (Figure 3.10).

The spheres represent lymph nodes and can be filled with a radioactive solution (Figure 3.10a). Using data from real sentinel lymph node biopsies the spheres are at positions which reflect the positions in the real biopsies. The declipse SPECT system from SurgicEye GmbH (Munich, Germany) was used to acquire scans of that phantom.
In the first set of experiments two hollow spheres with a radius of 5mm were each filled with 0.5 MBq Tc99m and placed in the phantom at a center-to-center distance of 14mm (Figure 3.10b). This represents a case of lymph nodes in very close proximity to each other where it is very hard to distinguish between them. Then six data sets with different acquisition geometries were acquired with the Freehand SPECT system. In the first data set only one side of the box was scanned, the number of sides scanned was then increased until all six sides were scanned in the last data set. Scans were performed by moving the probe freehanded along the sides of the phantom. Independent from the acquisition geometry the each scan used 3000 measurement points and took about three minutes. In this set of experiments the influence of different acquisitions geometries as well as the ability of the models to resolve two source very close to each other in the reconstructions was investigated.
Another set of experiments was conducted to investigate reconstructions with the different

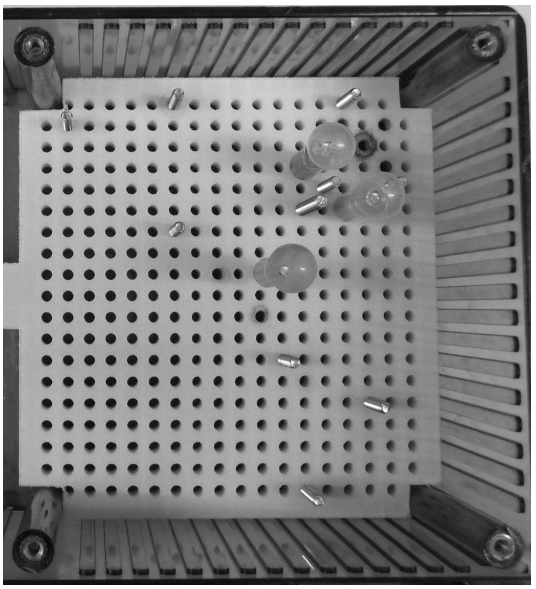

Figure 3.11: In a second set of experiments three hollow spheres were used and the box was filled with water with different levels of background radiation.

models in settings with different levels of background radiation. In this set of experiments three hollow spheres with a 5mm radius were filled with a radioactive solution of Tc99m with an activity of 0.35MBq each (Figure 3.11). The box with the spheres was then filled with radiated water with different levels of activity concentrations. The respective sphere-to-background activity ratios used were 30:1, 20:1, 10:1 and 5:1. For these experiments again a scan length of three minutes and 3000 measurement points was used while all scans covered the same three sides of the phantom (see Figure 3.10b, configuration 3).

3.4.3 Evaluation

The task of Freehand SPECT during the sentinel lymph node biopsy procedure is to detect the radioactive nodes and guide the surgeon to these nodes. For this task reconstructions are usually only regarded as binary images, using thresholding, to locate regions with high activity (i.e. the sentinel lymph nodes). For this task it should be as easy as possible for the surgeon to find a good threshold to locate the nodes. This is the case if there is a large range of thresholds where the nodes are located as good as possible. From pre-operative data the number of nodes as well as their rough position is known. This information is compared to the Freehand SPECT reconstruction for the detection of the nodes, making the process simple as long as all nodes are reconstructed and only few artifacts occur. To guide the surgeon during the procedure, the position of the reconstructed nodes has to be as accurate as possible with as few reconstruction artifacts as possible. For the evaluation of the task based performance for SLNB we thus consider the number of reconstructed nodes,

the artifacts and the position of the reconstructed nodes. If we get more reconstructed objects than real objects (the correct number is obtained from the known ground truth), some of the reconstructed objects are artifacts. The reconstructed objects that are closest to the real objects would be helpful for the task of guiding the surgeon, while the other objects would make the guidance more difficult. Thus we consider the superfluous objects which are the farthest from the real objects to be the artifacts as they would disturb the guidance of the surgeon. Artifacts disturb the guidance of Freehand SPECT depending on their size and their distance to the real nodes. For the error value of the artifacts (err_a) we divide the number of the voxels of each artifact (s_a) by the mean size of the detected nodes in voxels ($\overline{s}_n$) and their distance from the closest node in mm (d_{an}):

$$err_a = \frac{s_a}{\overline{s}_n d_{an}}. \tag{3.15}$$

The error in the position (err_p) of the reconstructed nodes is the most important parameter as it has the strongest influence on the quality of the guidance the Freehand SPECT system offers. We measure the position error by taking the difference in mm of the position of the nodes in the ground truth ($\vec{p_{gt}}$) and the position of the weighted centroid of the nearest nodes in the reconstruction ($\vec{p_{rec}}$):

$$err_p = \left|\vec{p_{gt}} - \vec{p_{rec}}\right|. \tag{3.16}$$

As the computed errors depend on the used thresholding, these errors are computed for different thresholds (t) of the reconstruction. We then obtain a graph for the error in position and of the artifacts depending on the threshold. For the thresholding, the intensity values of the reconstruction are normalized to values between 0 and 1. For each threshold, all values below the threshold are set to 0 and all above to 1, this is done in increments of 0.1 for the threshold.

3.4.4 Results

The acquired data was processed with the two models described in the previous section and with both a look up table from real measurements and a look up table generated with Gate. The resulting inverse problem was solved using MLEM with 20 iterations (more iterations do not improve the quality of the reconstruction, see Figure 3.13) and a voxel size of 2x2x2mm^3 in a volume of 40x35x25 voxels to obtain reconstructions of the activity distribution.

A first finding is that the scans of each data set produce very similar reconstructions, although the scans themselves always differ, as it is not possible to exactly reproduce a previous scan due to manual scanning (see Figure 3.14).

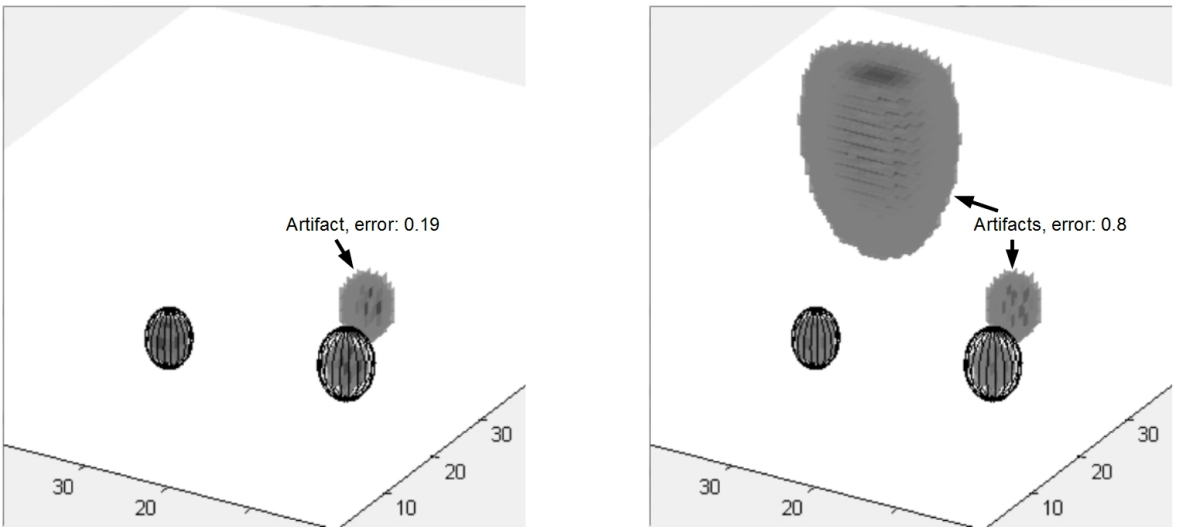

Figure 3.12: Two reconstructions of two nodes (black spheres) with one artifact (left, error value 0.19) and two artifacts (right, error value 0.8).

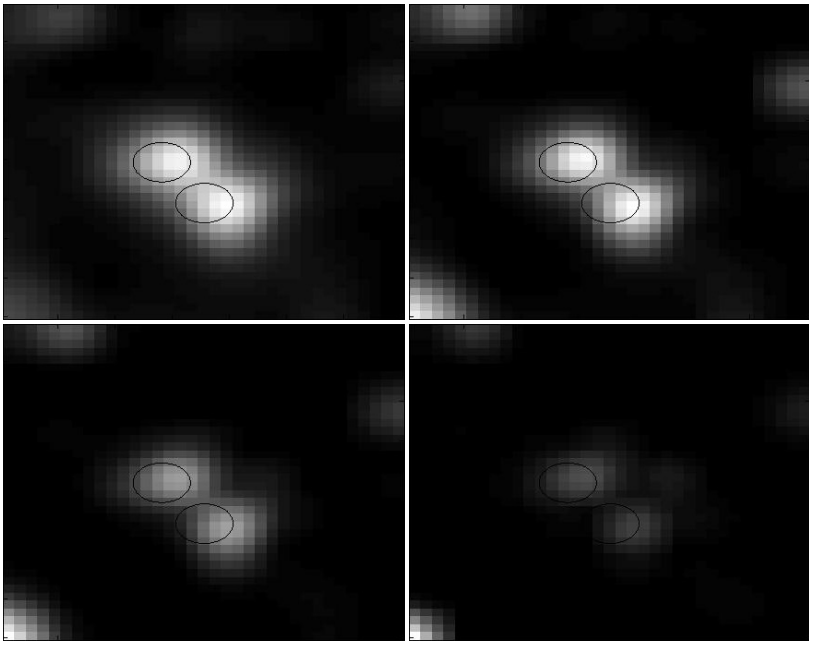

Figure 3.13: Reconstructions with 20, 50, 100 and 1000 iterations. The nodes are clearly visible with 20 iterations, further iterations only intensify the artifacts on the borders of the volume.

In a real clinical application the access to the volume of interest is usually limited, the results of the first set of experiments give us an idea of the necessary angle coverage. The reconstructions from the first experiment (See Figure 3.15) using the datasets with only one side of the phantom scanned did not produce useful reconstructions. With two sides of the phantom scanned, all models except for the solid angle model, reconstructed activity at approximately the correct position. With at least three sides covered in the scan both spheres could be reconstructed with all three models. However the results did not further

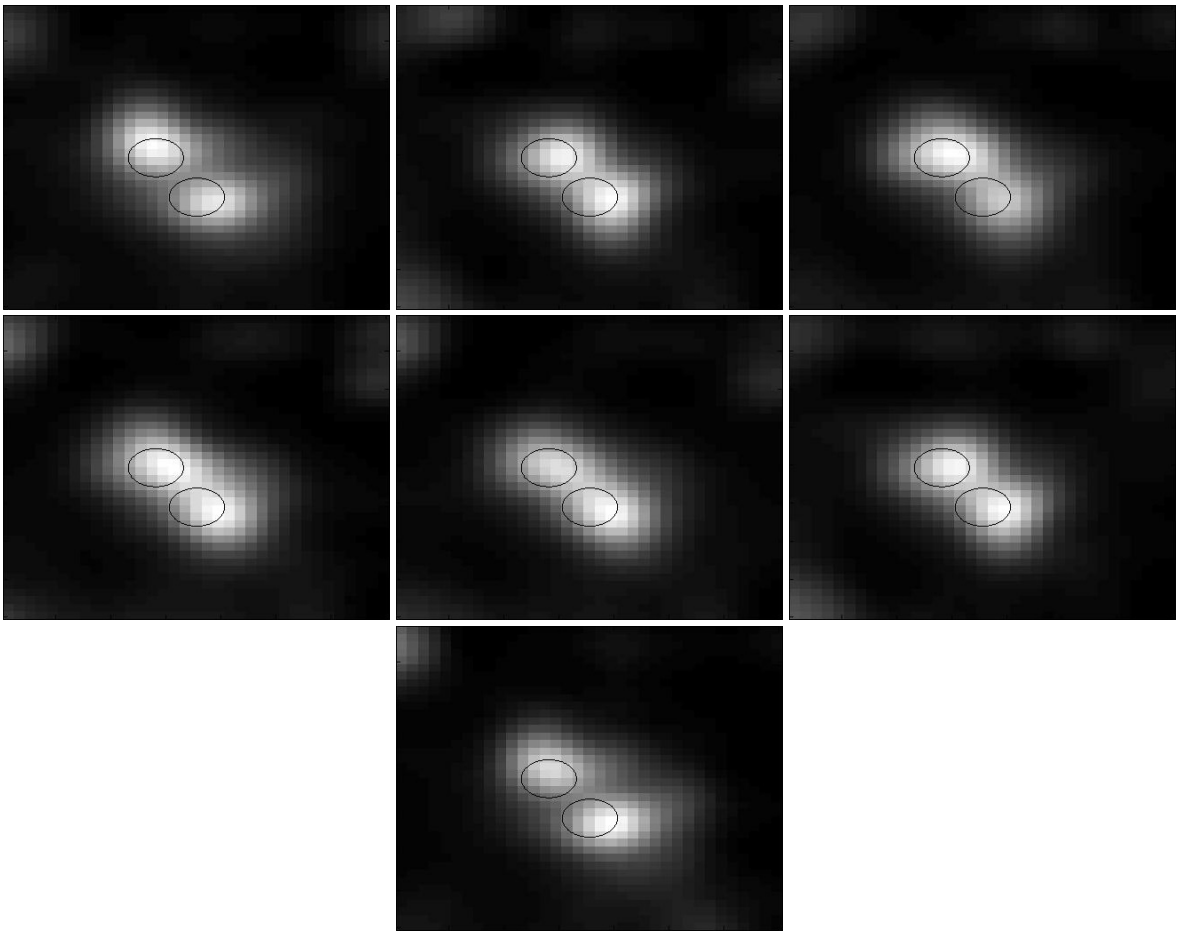

Figure 3.14: Results of the reconstructions of the seven scans of the data set for config. 3 are shown as slices from a top down view on the phantom, the circles indicate the positions of the spheres. Although the scans differ and are not reproducible, the results are very similar for every reconstruction.

improve by scanning more than three sides.

We evaluate position (err_p) and artifact error (err_a) for different thresholds (see Figure 3.16). The solid angle model performed worst in resolving the correct position, the minimum error in position achieved with the mo1del was 6.5mm. Reconstructions with the partition model, the look up table of real measurements and GATE-simulated measurements were equally good with minimum errors in the sphere center positions of about 4.8mm. The solid angle model and the look up table generated from real measurements produced fewer artifacts than the partition model and the look up table generated with Gate (Figure 3.16). See Figure 3.15 for a visual comparison. The separation of the nodes in the reconstruction can be further seen in a line profile through the centers of both nodes (Figure 3.17).

In the second experiments the spheres could be reconstructed from all data sets. The solid angle model was again the least accurate with a minimum error of 6.9mm in the sphere center positions. The other models performed again equally well with minimum errors in the sphere

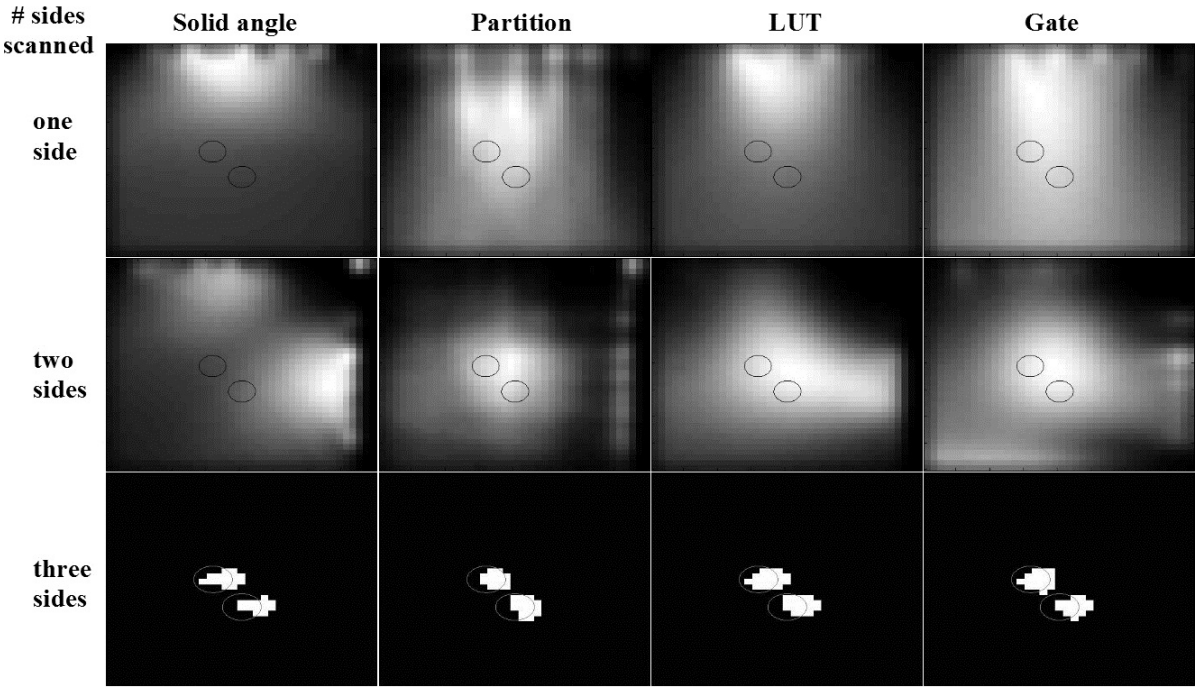

Figure 3.15: The results of the reconstructions are shown as slices from a top down view on the phantom, the circles indicate the positions of the spheres. In the first column the reconstructions of the solid angle model are shown, in the second the partition model, in the third the look up table of real measurements and in the fourth the look up table generated with Gate. The first row shows reconstructions of config. 1, the second of config. 2 and the third of config. 3. With config. 3 the spheres could be resolved with an appropriate threshold (fourth row).

center position of about 4.9mm. The background radiation did not affect the accuracy in the positions of the spheres but it introduced more artifacts in the reconstructions with higher levels of background radiation. With the partition model and the Gate generated look up table the more artifacts were produced (Figure 3.18).

The time required for the reconstructions was also measured using the data sets from the experiments, as the speed of a reconstruction is also critical for the application of Freehand SPECT during surgery. Using the solid angle model and the look up tables generated from real measurements and from a Gate simulation, the reconstructions took about 30s. The reconstructions using the partition model, however took significantly more time (3 minutes) as was expected due to its complexity. By generating a precomputed look up table from the partition model, the time required for a reconstruction with the partition model can be drastically reduced.

Using look up tables introduces however an additional error, as we need to interpolate between its entries. This error depends on the resolution of the look up table. In order to evaluate that error when using look up tables in the reconstruction process, look up tables of the solid angle model and the partition model were generated with 0.25mm, 1mm

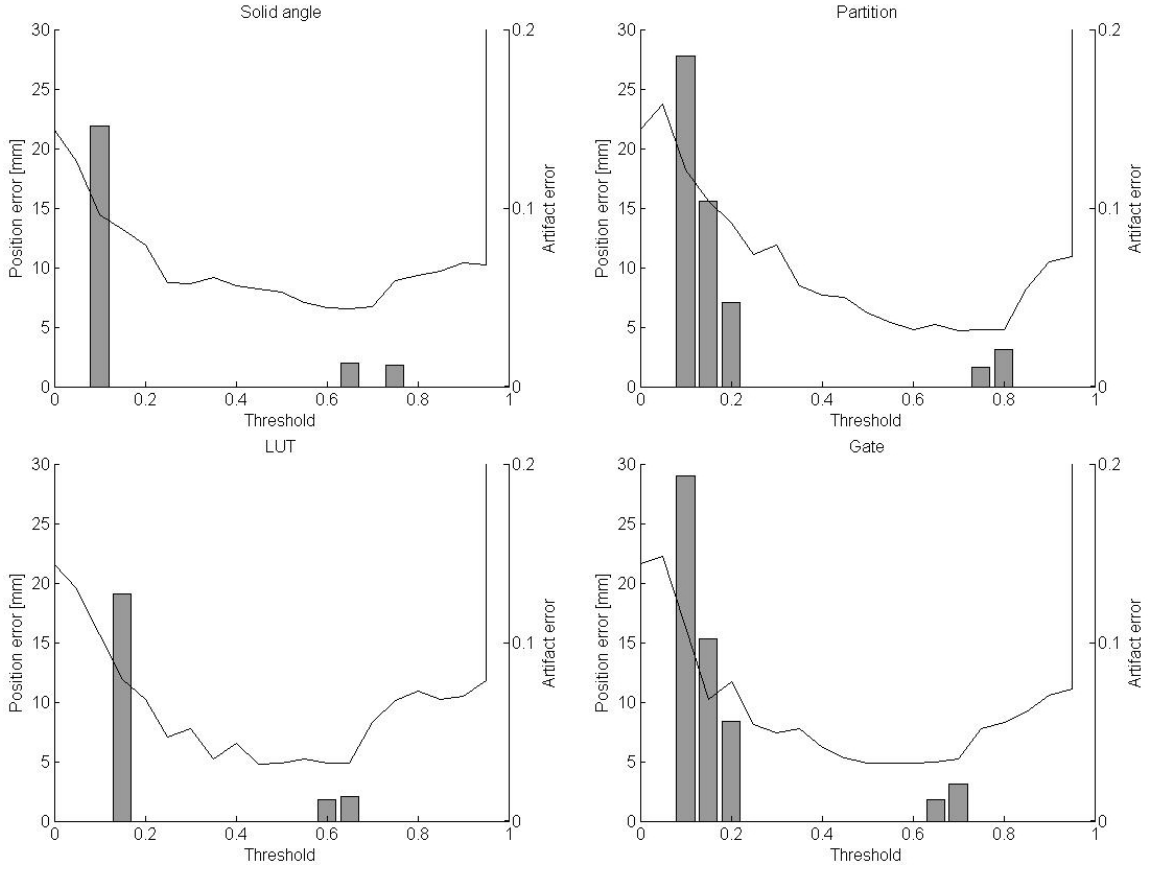

Figure 3.16: The resulting errors in position of the first set of experiments are shown in graphs for different thresholds for all models. In addition the bar graphs show the errors for the artifacts in the reconstruction.

and 4mm step sizes. These look up tables were then used for reconstruction of the data sets obtained from the experiments, with a voxel size of 2x2x2mm^3. The reconstructions using these look up tables were then compared to the reconstructions using their respective models by means of Normalized Cross Correlation (NCC). All reconstructions using the look up tables achieved a NCC of more than 95%. The look up tables with a step size of 1mm yielded a NCC higher than 99%. The reconstructions were only slightly further improved with a step size of 0.25mm. These results show that a step size of 1mm for the look up table is sufficiently accurate for reconstructions with a 2x2x2mm^3 voxel size.

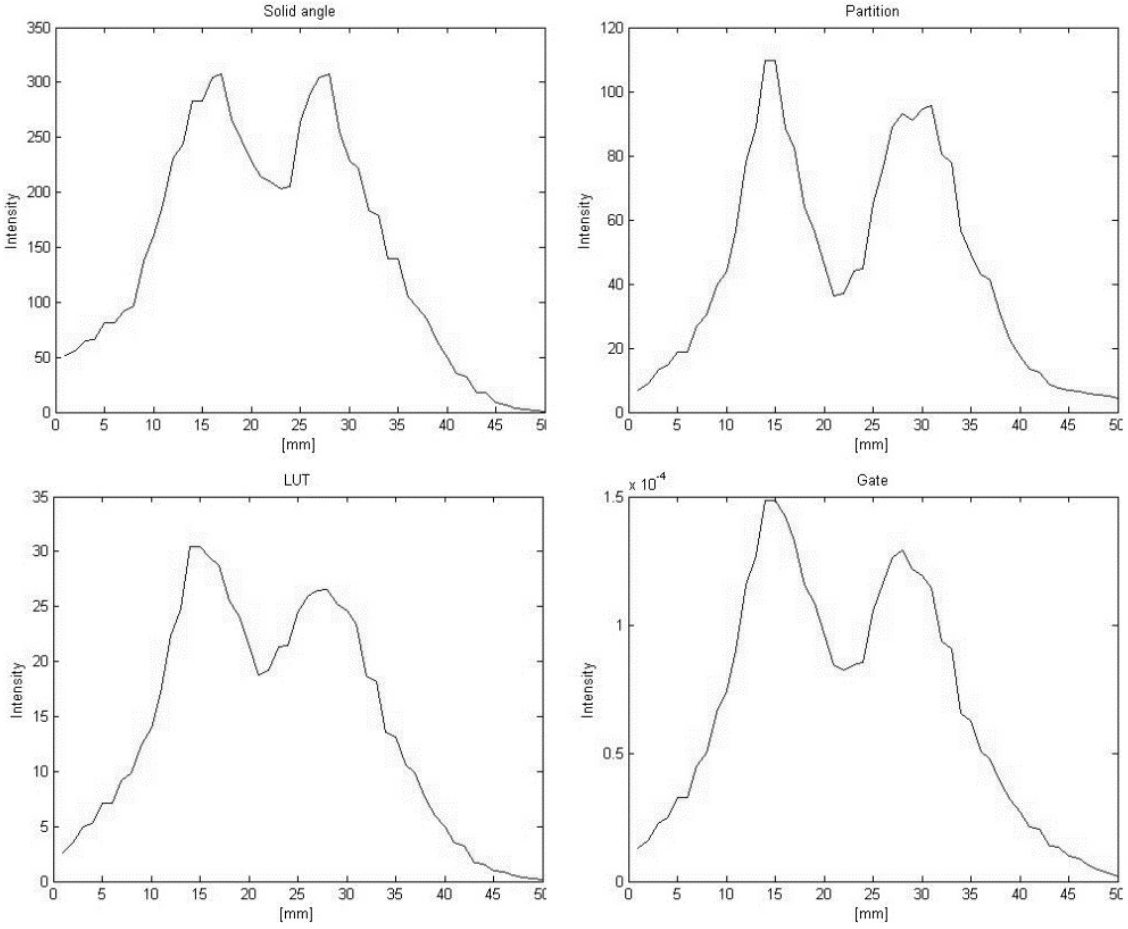

Figure 3.17: Plots through the centerlines of the reconstructed nodes of config. 3.

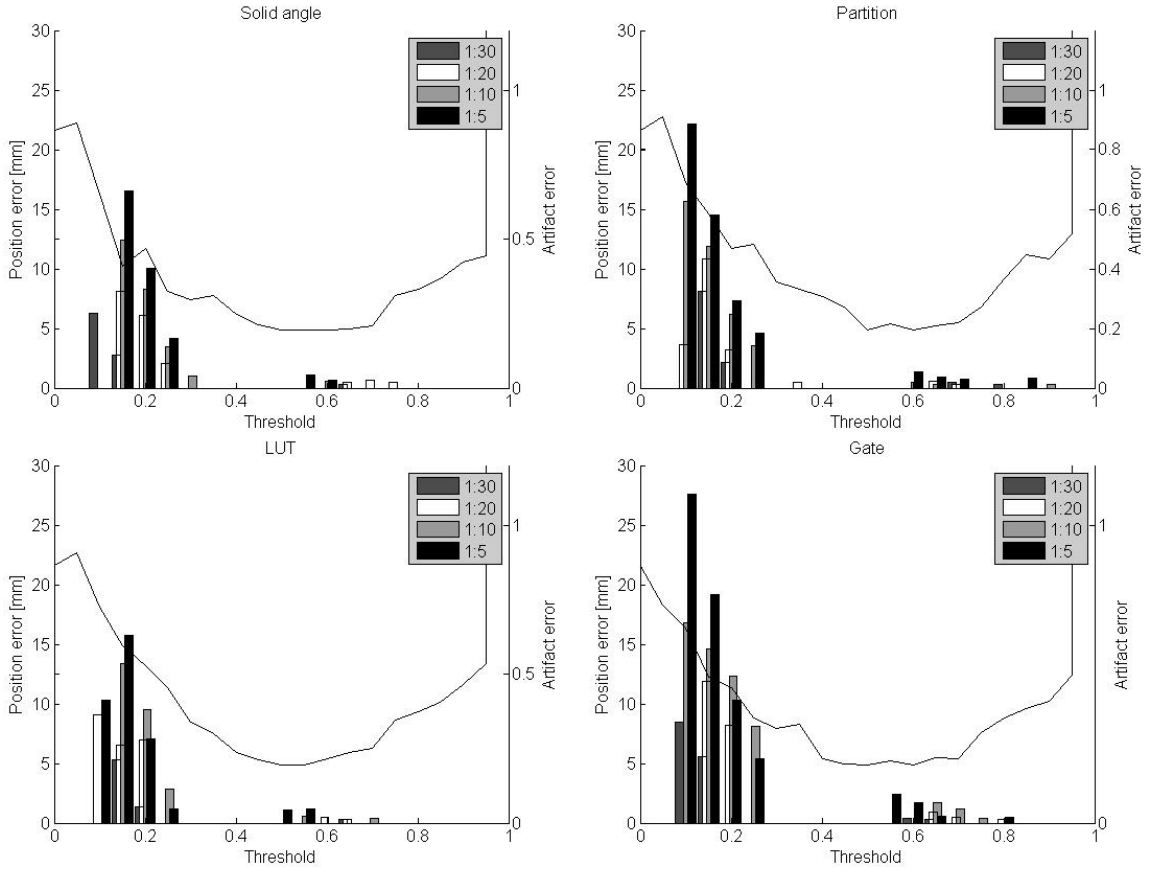

Figure 3.18: The resulting errors in position of the second set of experiments are shown in graphs for different thresholds for all models. In addition the bar graphs show the errors for the artifacts for different levels of background radiation.

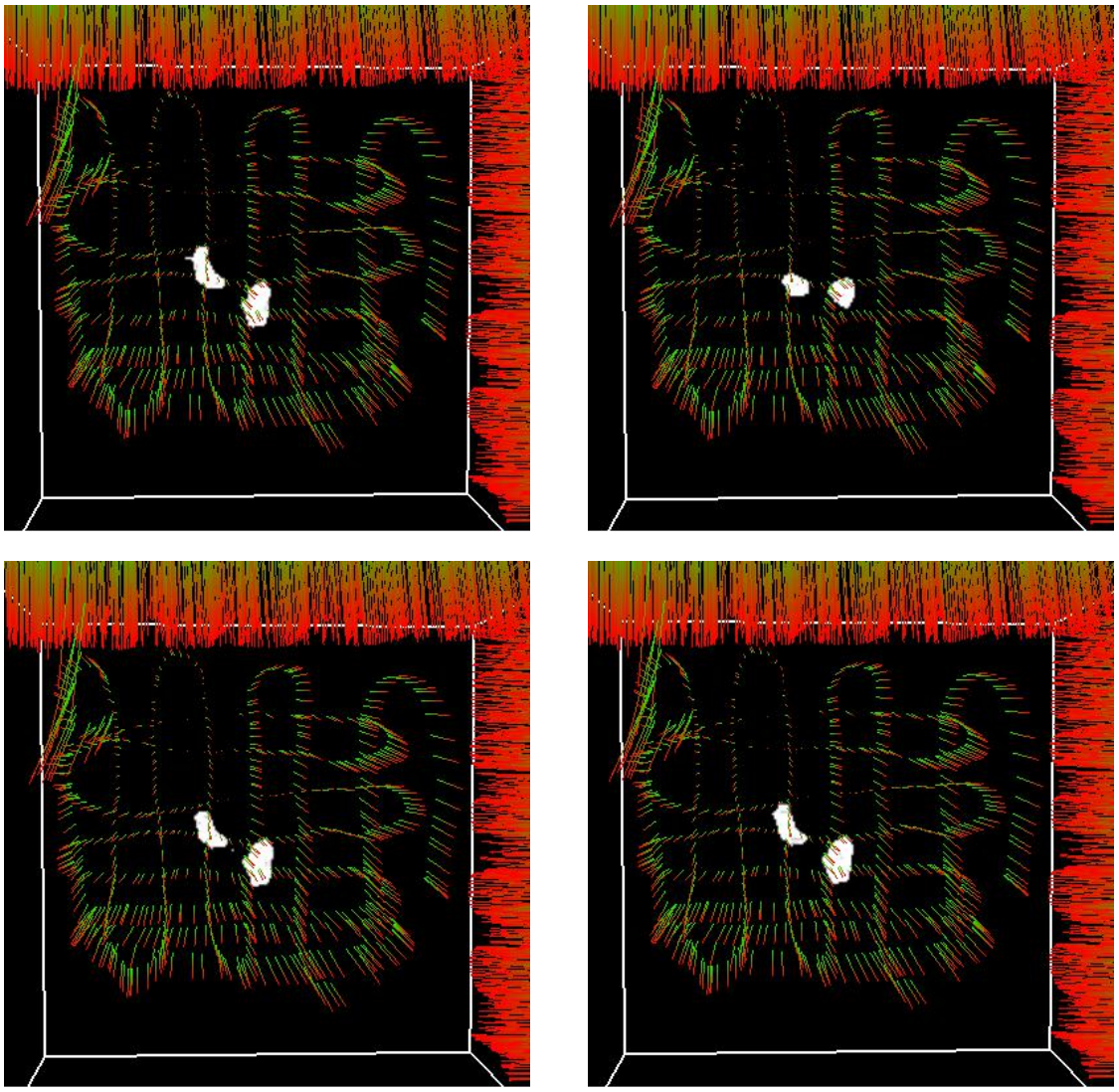

Figure 3.19: Reconstructions with the solid angle model and three look up tables generated from the solid angle model.

Chapter 4

Simulating and optimizing acquisition geometries

From the freehand acquisitions in Freehand SPCET not only arises the problem that the system matrix has to be build up on the fly but also that reconstructions are highly dependable on the way the acquisition is performed.
Due to the limitations during an intervention it is not possible to acquire measurements with a full angle coverage. This results in a very ill posed problem to be solved for a tomographic reconstruction and only a good acquisition geometry can give us a reasonable reconstruction. Furthermore it is not possible to reproduce freehand acquisition geometries.
A way to deal with these problems could be achieved with prior knowledge from preoperative images. By using preoperative data the acquisition can be planned beforehand and a good acquisition geometry can be defined before the acquisition. With simulations this acquisition geometry can then be validated and further optimized and with the use of a flexible robotic arm the predefined acquisition geometry can be executed precisely and independent of the user. That way it is possible to get images during surgery that were optimized specifically in regards to the patient and his disease.

4.1 Simulation of Freehand SPECT

We can simulate Freehand SPECT to observe results under different settings without the need to conduct experiments. These simulations can especially be used for an optimization process of the acquisition geometry. The simulation of Freehand SPECT consists effectively only of the simulation of the acquisition of the measurements, the reconstructions are then performed as with real measurements.
To simulate the measurements the positions and orientations of the probe have to be defined

as well as the positions and the amount of activity of the sources. In addition any intervening material has to be defined. Last a model of the detection process is required to simulate the measurements, for that we can use the models of the detection physics described in the previous section. In that case if we use the same model for the simulation and reconstruction we have a perfect model for the reconstruction process, so any errors in the reconstruction have to be from other sources than the model. This is very useful to investigate the errors resulting from the acquisition geometry and therefore for the optimization of it.
Another way to simulate Freehand SPECT is by using the Monte Carlo simulation framework GATE.

4.1.1 GATE

GATE is a Monte Carlo simulation framework designed to simulate PET and SPECT imaging systems. It is based on the Geant4 (later Geant5) simulation platform for the interaction of particles with material. The physical effects are simulated very accurately in Gate and the Monte Carlo simulation approach allows to simulate very complex system setups.
Using a set of instructions following the object oriented paradigm macros can be implemented to set up the different aspects of a simulation. In a first step all geometrical objects are defined and placed into the simulation volume and their physical properties are set. The objects working as detector are defined as well as all physical effects that are considered. In a last step the sources and their type are defined and placed in the simulation volume.
With Gate we can then simulate a whole Freehand SPECT scan with all desired effects to obtain a set of measurements for the reconstruction. Another advantage is that we also get correct statistical effects for the measurements if we want to investigate these too.

4.2 Error measure for reconstructions

Based on the idea of the figures of merit [45] a measure of error for reconstructions is defined for the optimization process. This figure of merit is defined according to the use of Freehand SPECT as an intra–operative guidance tool. As such, reconstructions are usually only regarded as binary images, using thresholding, to locate regions with high activity. In a first step the most important factors that compose a good reconstruction were found by analyzing the results of different errors in reconstructions. Four different types of errors were found, which influence the use of the reconstruction as an intra operative guidance: position, artifacts, size and shape.

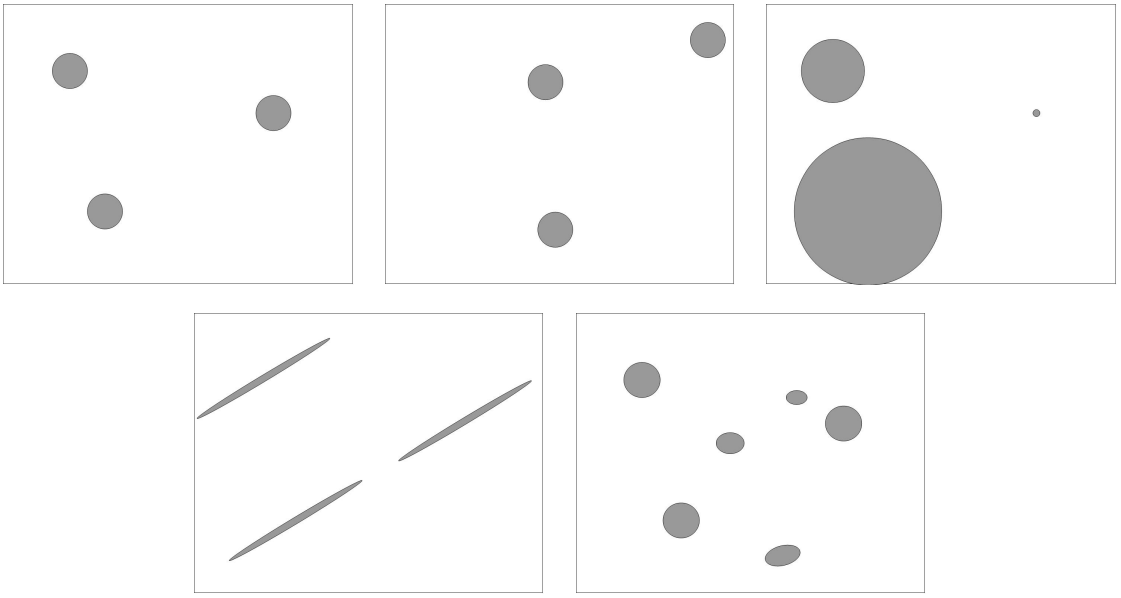

Figure 4.1: Four different types of errors influence the quality of a reconstruction.(a) Ground truth, (b) error in position, (c) error in size, (d) error in shape, (e) artifacts

To compute these errors the reconstruction is analyzed with different thresholds. For each threshold each resulting reconstructed objects is compared with all ground truth objects to determine which reconstructed objects match best to the ground truth objects. With this comparison the different errors can then be computed. The position error (err_p) is determined by simply computing the difference in the positions of the reconstructed ($\vec{p_{rec}}$) and ground truth ($\vec{p_{gt}}$) objects.

$$err_p = \|\vec{p_{gt}} - \vec{p_{rec}}\|_2 \tag{4.1}$$

The error in size (err_s) is computed by taking the absolute difference between the number of voxels of the ground truth object (v_{gt}) and the reconstructed object (v_{rec}) and dividing it by the number of voxels of the ground truth object.

$$err_s = \frac{|v_{gt} - v_{rec}|}{v_{gt}} \tag{4.2}$$

For the error in shape (err_{sh}), the ground truth objects are first rescaled to match the size of the reconstructed object. Then the objects are overlayed and the dice coefficient [46] is computed by dividing the number of voxels the two objects have in common (v_{oc}) by the mean number of voxels of these two objects ($\overline{v_o}$). The error value is then one minus the dice coefficient.

$$err_{sh} = \frac{v_{oc}}{\overline{v_o}} \tag{4.3}$$

Using these three error values for every threshold the best matching between reconstructed and ground truth objects is determined. All reconstructed objects that are not matched to a ground truth object are now considered to be artifacts. Their summed up size in voxels (v_a) multiplied with their mean intensity value ($\bar{i}$) gives us then the error value for the artifacts (err_a).

$$err_a = \frac{v_a \bar{i}}{v_m} \tag{4.4}$$

Finally for every ground truth object, the smallest error value is taken from all thresholds and the summed up error values give us a measure of error for the reconstruction. Thus high error measures indicate a bad reconstruction quality.
However, as the four errors in position, size, shape and artifacts affect the quality of the reconstruction differently and are not comparable among each other, it is necessary to weight them appropriately before they are added up. To obtain these weights (w_*), five freehand acquisition experts were asked to rate twelve different sets of six reconstructions in terms of their quality. Using these ratings appropriate weights were determined by iteratively choosing weights and adjusting them until the measure of error matched the ratings.

$$err = w_p err_p + w_s err_s + w_{sh} err_{sh} + w_a err_a \tag{4.5}$$

In addition nodes that are not reconstructed at all are penalized with a flat error value of 100.

4.3 Optimization process

The optimization process starts with setting up a Freehand SPECT simulation. By using the preoperative data the geometrical context is set and the sources are defined. This setup is then used for all simulations during the optimization.
Next the scanning geometry is defined, for that either a predefined initial geometry is used or a random geometry is generated.
With the setup and the scanning geometry defined a Freehand SPECT simulation can be started. The resulting measurements are then used to perform a reconstruction. Using the preoperative data an error measure of the reconstruction can then be computed. The error measure of the reconstruction is used as the costfunction in the optimization. Then the

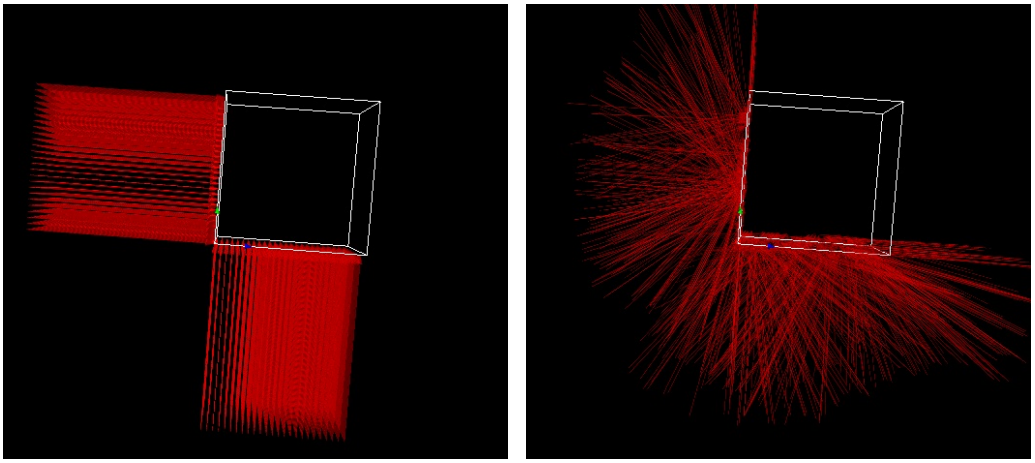

Figure 4.2: The acquisition geometry for a one setup before the optimization (left) and after the optimization process (right).

acquisition geometry is changed by replacing a user defined percentage of the measurement poses with random poses. With the new acquisition geometry a new simulation is started and the process is repeated. If the error measure does not decrease the percentage of measurement points which are replaced is increased. This process is repeated until the error measure does not decrease after several iterations with the whole set of measurements being replaced.

4.4 Experiments and results

4.4.1 Simulations

For a first evaluation of the optimization of the acquisition geometry a set of simulations was performed. For the simulation a cube with 10x10x10cm was defined. In this box three, four and five spherical sources were placed at different positions with different activity levels. Only two sides of the box were accessible for these experiments to reflect the intra operative setting where the access to the volume of interest is also very restricted. Starting with a uniform scanning scheme spread over both accessible sides of the box the acquisition geometry was optimized in 1000 iterations of the algorithm described in 4.

4.4.2 Results

Beginning with the uniform scanning scheme the acquisition geometry was changed to a more optimal for the specific setup (Figure 4.2)

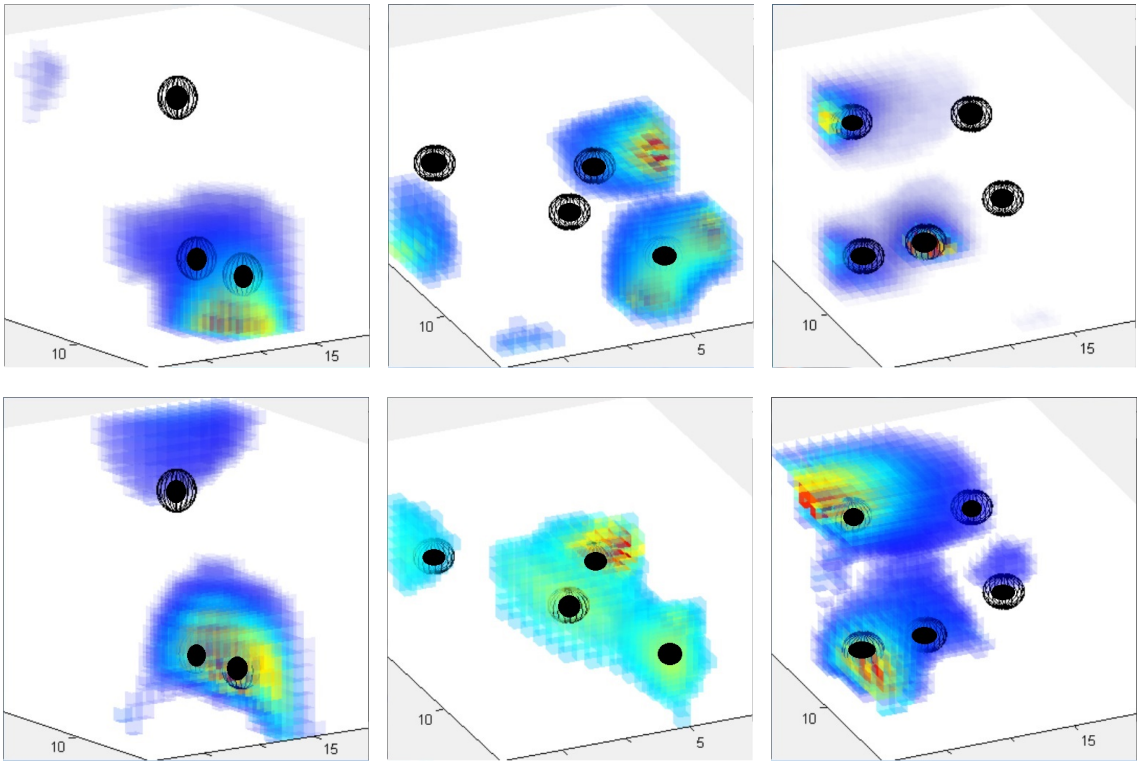

Figure 4.3: Results of the optimization process. In the first row reconstructions before the start of the optimization are shown and in the second row the results after 1000 iterations. From left to right 3, 4 and 5 nodes were used in the ground truth, which is shown as the black spheres.

Over the optimization process the error value improved from values around 200 to values of 5 and below. Visually the reconstructions also improved, as can be seen in Figure 4.3. Especially nodes that were not reconstructed at all in the beginning of the optimization process could be reconstructed afterwards.

Chapter 5

Discussion and Conclusions

5.0.3 Discussion

Each of the proposed models has certain advantages and disadvantages. The solid angle model is computationally fast and easy to apply to every handheld detector (probe), as only the dimensions of the detector are needed. However due to its simplicity, its results are less accurate than those of the other models. The partition model has to be redeveloped for each probe as the differences in the geometric design are usually too big to simply adapt it for a new probe. As the computations are much more complex, it is also by far the slowest of the proposed models but produces very accurate reconstructions. In order to obtain a look up table using real measurements, additional hardware is required for the acquisition. A precision positioning system to acquire the measurements at all positions is required to get an accurate look up table. Note that in this case the acquisition can take up to several days. If the hardware is available, the look up table is the easiest way to obtain a model for a new probe. However for the acquisition of the measurements it is difficult to place a small source in the correct relative position to a probe and in addition it is not possible to have a real point source as it will always have a non-infinitesimal extent. Improvements in these points might yield better look up tables with which better reconstructions could be possible. Look up tables generated with GATE also produce very accurate reconstructions, however the necessary simulations require a lot of computing power and time. Using one CPU with 2.6GHz such a simulation would take about 4 months, but the simulation can easily be parallelized to reduce this computational time.
Different optimizers could be used for the optimization of the acquisition geometry to achieve better results. For a better evaluation real experiments are required.

5.0.4 Conclusions

In this work we evaluated different models for the use in Freehand SPECT reconstructions. Freehand SPECT is the first intra-operative solution for functional tomographic imaging and comes with specific requirements in accuracy, speed and flexibility. The proposed models can compute the system matrix very fast on the fly, which is required for freehand acquisitions, as it is not possible to precompute the system matrix like in conventional tomography. Analyzing the properties of the models is therefore a crucial work in the development of such a system. With all models a sufficient accuracy in the reconstruction could be achieved to guide a surgeon to the lymph nodes in a sentinel lymph node biopsy. We showed that it is possible to perform reconstructions with a very simple analytical model, but with more complex modeling the accuracy of the reconstruction is improved. Look up tables from real measurements of the probe and measurements generated with Gate are superior to the simple analytical model as expected. We also showed that with a more complex analytical model, reconstructions with a similar quality to the look up tables from GATE and real measurements can be computed. Such a model can also be used to generate a look up table to improve the speed of the reconstruction. The use of look up tables generated from either real measurements (M3), Monte Carlo simulations (M4) or simulations of a complex analytical model ($M2_{lut}$), is a good solution for generating the system matrix in Freehand SPECT, as they are fast and offer a good accuracy.
The optimization of acquisition geometries seems a promising approach to achieve better reconstruction results when the setup for the reconstruction fits for such an approach (e.g. a robot for the acquisition process is required).

Appendix A

List of Publications

Over the course of this work several publications were created. Here is a list, current as of 10 May 2015.

A.1 Submitted Journal Publications

A. Hartl, Dzhoshkun I. Shakir, Tobias Lasser, S.I. Ziegler and N. Navab. Detection models for Freehand SPECT reconstruction. In *Physics in medicine and biology*, 60(3):1031-46, February 2015.

A.2 Conference publications

2013

A. Okur, D. I. Shakir, P. Matthies, **A. Hartl**, M. Essler, S. I. Ziegler, T. Lasser, N. Navab. Freehand Tomographic Nuclear Imaging Using Tracked High-Energy Gamma Probes. In *Bildverarbeitung fr die Medizin 2013 (BVM)*, Heidelberg, Germany, March 2013.

2012

D. I. Shakir, A. Okur, **A. Hartl**, P. Matthies, M. Essler, S. I. Ziegler, T. Lasser, N. Navab. Towards Intra-operative PET for Head and Neck Cancer: Lymph Node Localization Using High-energy Probes. In *Proceedings of the 15th International Conference on Medical Image Computing and Computer Assisted Interventions (MICCAI)*, Nice, France, October 2012.

A. Hartl, D. I. Shakir, R. Kojchev, N. Navab, S. I. Ziegler, T. Lasser. Freehand SPECT reconstructions using look up tables. In *SPIE Medical Imaging Conference, San Diego, USA, February 2012.*

D. I. Shakir, **A. Hartl**, F. R. Schneider, J. Pulko, S. I. Ziegler, N. Navab, T. Lasser. Two new ad-hoc models of detection physics and their evaluation for navigated beta probe surface imaging. In *Proceedings of SPIE Visualization, Image-Guided Procedures, and Modeling Conference*, San Diego, CA, USA, February 2012.

2011

A. Hartl, T. Lasser, N. Navab, S. I. Ziegler. Impact of acquisition geometry and physical model on Freehand SPECT reconstructions. In *IEEE Medical Imaging Conference*, Valencia, Spain, October 2011

D. I. Shakir, **A. Hartl**, N. Navab, S. I. Ziegler. Evaluation of an ad hoc model of detection physics for navigated beta-probe surface imaging. In *Proceedings of SPIE Visualization, Image-Guided Procedures, and Modeling Conference*, Lake Buena Vista, USA, February 2011.

2010

A. Hartl, N. Navab, S. I. Ziegler. Models of detection physics for nuclear probes in free-hand SPECT reconstruction. In *IEEE Medical Imaging Conference*, Knoxville, Tennessee, November 2010.

A. Hartl, N. Navab, S. I. Ziegler. Comparison study of detection models for nuclear probes. In *Annual Congress of the European Association of Nuclear Medicine*, Vienna, Austria, October 2010.

2009

A. Hartl, Z. Yaniv. Evaluation of a 4D Cone-Beam CT Reconstruction Approach using a Simulation Framework. In *Proceedings of IEEE Engineering in Medicine and Biology Conference*, Minnesota, USA, September 2009.

A. Hartl, Z. Yaniv. A comparison study of two reconstruction methods for gated Cone-Beam CT. In *Proceedings of Computer Assisted Radiology and Surgery (CARS2009)*, Berlin Germany, June 2009

2008

T. Wendler, **A. Hartl**, T. Lasser, J. Traub, S. I. Ziegler, N. Navab. Tracking-based statistical correction for radio-guided cancer surgery. In *Proceedings of World Molecular Imaging Congress (WMIC 2008)*, Nice, France, September 2008.

T. Wendler, **A. Hartl**, T. Lasser, J. Traub, S. I. Ziegler, N. Navab. 3D Intra-operative nuclear imaging for SLNB in neck. In *Proceedings of Annual Meeting of Society of Nuclear Medicine (SNM 2008)*, New Orleans, USA, June 2008

A. Hartl, T. Wendler, J. Traub, T. Lasser, S. I. Ziegler, N. Navab. Confident radioactivity surface reconstruction for control of resection borders. In *Proceedings of Annual Meeting of Society of Nuclear Medicine (SNM 2008)*, New Orleans, USA, June 2008.

2007

T. Wendler, **A. Hartl**, T. Lasser, J. Traub, F. Daghighian, S. I. Ziegler, N. Navab. Towards intra-operative 3D nuclear imaging: reconstruction of 3D radioactive distributions using tracked gamma probes. In *Proceedings of Medical Image Computing and Computer-Assisted Intervention (MICCAI 2007)*, Brisbane, Australia, October 2007

A. Hartl, T. Wendler, T. Lasser, J. Traub, S. I. Ziegler, N. Navab. Towards intra-operative 3D nuclear imaging: development and evaluation of ad hoc models. In *Proceedings of Jahrestagung der deutschen Gesselschaft fr Computer- und Roboterassistierte Chirurgie e.V. (CURAC 2007)*, Karlsruhe, Germany, October 2007.

T. Wendler, J. Traub, **A. Hartl**, T. Lasser, M. Burian, A. K. Buck, F. Daghighian, M. Schwaiger, S. I. Ziegler, N. Navab. Adding navigation to radio-guided surgery: new possibilities, new problems, new solutions. In *Proceedings of Russian Bavarian Conference on Biomedical Engineering (RBC Biomed 2007)*, Erlangen, Germany, July 2007

T. Wendler, **A. Hartl**, J. Traub, S. I. Ziegler, N. Navab. Intraoperative nuclear imaging using navigated gamma-probes for tumor localization. In *Proceedings of Annual Meeting of Society of Nuclear Medicine (SNM 2007)*, Washington D.C., USA, June 2007

Bibliography

[1] W. C. Röntgen, "Ueber eine neue Art von Strahlen. (Vorläufige Mittheilung)." *Aus den Sitzungsberichten der Würzburger Physik.–medic. Gesellschaft*, 1895.

[2] G. Hounsfield, "Computerised transverse axial scanning (tomography): Part 1. Description of system," *Br. J. Radiol.*, vol. 46, pp. 1016–1022, 1973.

[3] A. Koch, C. Raven, P. Spanne, and A. Snigirev, "X-ray imaging with submicrometer resolution employing transparent luminescent screens," *Journal of the Optical Society of America*, vol. 15, pp. 1940–1951, 1998.

[4] J. J. Wild, "The use of ultrasonic pulses for the measurement of biological tissues and the detection of tissue density changes," *Surgery*, vol. 27, pp. 183–188, 1950.

[5] R. Damadian, "Tumor detection by nuclear magnetic resonance," *Science*, vol. 171, pp. 1151–1153, 1971.

[6] F. Daghighian, J. C. Mazziotta, E. J. Hoffman, P. Shenderov, B. Eshaghian, and S. Siegel, "Intraoperative beta probe: A device for detecting tissue labeled with positron or electron emitting isotopes during surgery," *Medical Physics*, vol. 21, pp. 153–157, 1994.

[7] P. Matthies, K. Sharma, A. Okur, J. Gardiazabal, J. Vogel, T. Lasser, and N. Navab, "Mini gamma cameras for intra-operative nuclear tomographic reconstruction." *Medical Image Analysis*, vol. 18, pp. 1329–1336, 2014.

[8] M. N. Wernick and J. N. Aarsvold, "Emission tomography. the fundamentals of pet and spect." *Academic Press*.

[9] B. H. Hasegawa and A. Frenkel, "Physics and history of spect/ct," *CRC Press*, 2006.

[10] K. Godfrey, "Compartmental models and their application," *International Journal of Bio-Medical Computing*, vol. 16, pp. 294–295, 1985.

[11] S. Matej, G. T. Herman, T. K. Narayan, S. S. Furuie, R. M. Lewitt, and P. E. Kinahan, "Evaluation of task-oriented performance of several fully 3d pet reconstruction algorithms," *Physics in Medicine and Biology*, vol. 39, pp. 355–367, 1994.

[12] P. P. B. Eggermont, G. T. Herman, and A. Lent, "Iterative algorithms for large partitioned linear systems, with applications to image reconstruction," *Linear Algebra Appl.*, vol. 40, pp. 37–67, 1981.

[13] A. Anderson and A. Kak, "Simultaneous algebraic reconstruction technique (sart): a superior implementation of the art algorithm," *Ultrason. Imaging*, vol. 6, pp. 81–94, 1984.

[14] G. T. Herman and L. B. Meyer, "Algebraic reconstruction techniques can be made computationally efficient [positron emission tomography application]," *IEEE Transactions on Medical Imaging*, vol. 12, pp. 600–609, 1993.

[15] T. Wendler, K. Herrmann, A. Schnelzer, T. Lasser, J. Traub, O. Kutter, A. Ehlerding, K. Scheidhauer, T. Schuster, M. Kiechle, M. Schwaiger, N. Navab, S. I. Ziegler, and A. K. Buck, "First demonstration of 3-D lymphatic mapping in breast cancer using freehand SPECT," *Eur. J. Nucl. Med. Mol. Imaging*, vol. 37, pp. 1452–1461, 2010.

[16] T. Wendler, A. Hartl, T. Lasser, J. Traub, F. Daghighian, S. I. Ziegler, and N. Navab, "Towards intra-operative 3d nuclear imaging: reconstruction of 3d radioactive distributions using tracked gamma probes," *Proc. Intl. Conf. on Medical Image Computing and Computer-Assisted Intervention (MICCAI)*, vol. 10, pp. 909–917, 2007.

[17] A. Rieger, J. Saeckl, B. Belloni, R. Hein, A. Okur, K. Scheidhauer, T. Wendler, J. Traub, H. Friess, and M. Martignoni, "First experiences with navigated radio-guided surgery using freehand spect," *Case Reports in Oncology*, vol. 4, pp. 420–425, 2011.

[18] D. Strul, R. B. Slates, M. Dahlbom, S. R. Cherry, and P. K. Mars, "An improved analytical detector response function model for multilayer small-diameter pet scanners," *Physics in medicine and biology*, vol. 48, pp. 979–994, 2003.

[19] M. S. Tohme and J. Qi, "Iterative image reconstruction for positron emission tomography based on a detector response function estimated from point source measurements," *Physics in medicine and biology*, vol. 54, pp. 3709–3725, 2009.

[20] D. Borys, K. Naszczucka-Borys, and K. Gorczewski, "System matrix computation for iterative reconstruction algorithms in spect based on direct measurements," *International Journal of Applied Mathematics and Computer Science*, vol. 21, pp. 193–202, 2011.

[21] Z. E. Bitar, D. Lazaro, C. Coello, V. Breton, D. Hil, and I. Buvat, "Fully 3d monte carlo image reconstruction in spect using functional regions," *Nuclear Instruments and Methods in Physics Research Section A: Accelerators*, vol. 569, pp. 399–403, 2006.

[22] E. Frey and B. M. W. Tsui, "Modeling the scatter response function in inhomogeneous scattering media for spect." *IEEE Transactions on nuclear science*, vol. 41, pp. 1585–1593, 1994.

[23] M. A. King, B. M. W. Tsui, T.-S. Pan, S. J. Glick, and E. J. Soares, "Attenuation compensation for cardiac spect imaging: Part 2. attenuation compensation algorithms." *Journal of Nuclear Cardiology*, vol. 3, pp. 55–63, 1996.

[24] S. C. Curran and J. D. Craggs, "Counting tubes: theory and applications," *Academic Press*, 1949.

[25] J. B. Briks, "The theory and practice of scintillation counting," *Pergamon Press*, 1964.

[26] E. Rutherford, "The origin of β and γ rays from radioactive substances," *Philosophical Magazine*, vol. 24, pp. 453–462, 1912.

[27] N. Bohr, "On the constitution of atoms and molecule," *Philosophical Magazine*, vol. 26, pp. 1–25, 1913.

[28] P. A. Tipler and R. Llewellyn, "Modern physics," *Wiley*, 2002.

[29] R. Harris, "Nonclassical physics," *Pearson*, 1999.

[30] A. Beiser, "Concepts of modern physics," *McGraw Hill*, 2003.

[31] A. Einstein, "über einen die erzeugung und versandlung des lichtes betreffenden heuristischen gesichtspunkt," *Annalen der Physik*, vol. 17, pp. 132–148, 1905.

[32] A. H. Compton, "X-rays in theory and experiment," *D. Van Nostrand Company*, 1935.

[33] J. J. Thomas, B. R. Thomas, and H. M. Overeynder, "Indoor radon concentration data: Its geographic and geologic distribution, an example from the capital district, ny," *International Radon Symposium*, 1995.

[34] U. N. S. C. on the Effects of Atomic Radiation, "Sources of ionizing radiation," *UNSCEAR 2008 REPORT Vol. I*, 2008.

[35] E. Frey and B. M. W. Tsui, "Collimator-detector response compensation in spect," *Quantitative Analysis in Nuclear Medicine Imaging*, pp. 141–166, 2006.

[36] R. L. Siddon, "Fast calculation of the exact radiological path for a three-dimensional ct array," *Medical Physics*, vol. 12, pp. 252–255, 1985.

[37] W. R. Martin, "Monte carlo methods on advanced computer architectures." *Advances in Nuclear Science and Technology*, vol. 22, pp. 105–164, 1991.

[38] P. Andreo, "Monte carlo techniques in medical radiation physics." *Physics in Medicine and Biology*, vol. 36, pp. 861–920, 1991.

[39] M. Ljungberg, "Monte-carlo calculations in nuclear medicine: second edition," *IOP Publishing*, 2012.

[40] S. Agostinelli, J. Allison, K. Amako, J. Apostolakis, H. Araujo, P. Arce, M. Asai, D. Axen, S. Banerjee, G. Barrand, F. Behner, L. Bellagamba, J. Boudreau, L. Broglia, A. Brunengo, H. Burkhardt, S. Chauvie, J. Chuma, R. Chytracek, G. Cooperman, G. Cosmo, P. Degtyarenko, A. Dell'Acqua, G. Depaola, D. Dietrich, R. Enami, A. Feliciello, C. Ferguson, H. Fesefeldt, G. Folger, F. Foppiano, A. Forti, S. Garelli, S. Giani, R. Giannitrapani, D. Gibin, J. J. G. Cadenas, I. Gonzalez, G. G. Abril, L. G. Greeniaus, W. Greiner, V. Grichine, A. Grossheim, P. Gumplinger, R. Hamatsu, K. Hashimoto, H. Hasui, A. Heikkinen, A. Howard, V. Ivanchenko, A. Johnson, F. W. Jones, J. Kallenbach, N. Kanaya, M. Kawabata, Y. Kawabata, M. Kawaguti, S. Kelner, P. Kent, T. Kodama, R. Kokoulin, M. Kossov, H. Kurashige, E. Lamanna, T. Lampen, V. Lara, V. Lefebure, F. Lei, M. Liendl, W. Lockman, F. Longo, S. Magni, M. Maire, E. Medernach, K. Minamimoto, P. M. de Freitas, Y. Morita, K. Murakami, M. Nagamatu, R. Nartallo, P. Nieminen, T. Nishimura, K. Ohtsubo, M. Okamura, S. O'Neale, Y. Oohata, K. Paech, J. Perl, A. Pfeiffer, M. G. Pia, F. Ranjard, A. Rybin, S. Sadilov, E. D. Salvo, G. Santin, T. Sasaki, N. Savvas, Y. Sawada, S. Scherer, S. Sei, V. Sirotenko, D. Smith, N. Starkov, H. Stoecker, J. Sulkimo, M. Takahata, S. Tanaka, E. Tcherniaev, E. S. Tehrani, M. Tropeano, P. Truscott, H. Uno, L. Urban, P. Urban, M. Verderi, A. Walkden, W. Wander, H. Weber, J. P. Wellisch, T. Wenaus, D. C. Williams, D. Wright, T. Yamada, H. Yoshida, and D. Zschiesche, "Geant4a simulation toolkit," *Nuclear Instruments and Methods in Physics Research Section A: Accelerators, Spectrometers, Detectors and Associated Equipment*, vol. 506, pp. 250–303, 2003.

[41] D. Strul, G. Santinc, D. Lazarod, V. Bretond, and C. Morelb, "Gate (geant4 application for tomographic emission): a pet/spect general-purpose simulation platform," *Nuclear Physics B Proceedings Supplements*, vol. 125, pp. 75–79, 2003.

[42] G. Santin, D. Strul, D. Lazaro, and L. Simon, "Gate, a geant4-based simulation platform for pet and spect integrating movement and time management," *IEEE Transactions on Nuclear Science*, vol. 50, pp. 1516–1521, 2003.

[43] P. Aguiar, F. Pino, J. Silva-Rodrguez, J. Pava, D. Ros, A. Ruibal, and Z. Bitar, "Analytical, experimental, and monte carlo system response matrix for pinhole spect reconstruction," *Medical Physics*, vol. 41, 2014.

[44] I. Buvat and I. Castiglioni, "Monte carlo simulations in spet and pet," *Q J Nucl Med.*, vol. 46, pp. 48–61, 2002.

[45] G. T. Herman, "Fundamentals of computerized tomography," *Springer-Verlag*, 2009.

[46] L. R. Dice, "Measures of the amount of ecologic association between species," *Ecology*, vol. 26, pp. 297–302, 1945.